Enhancing One-Equation Turbulence Models for Delta Wings by Gene Expression Programming

Enhancing one-equation turbulence models for delta wings by gene expression programming

Dario Kotzlowski, * Eike Tangermann † and Markus Klein ‡
University of the Bundeswehr Munich, Neubiberg, Germany, 85577

Tony Di Fabbio §
University of the Bundeswehr Munich, Neubiberg, Germany, 85577
Leonardo SPA Innovation Labs & IP, Digital Twin and Advanced Simulation, Genova, Italy, 16151

Yuan Fang ¶ and Richard D. Sandberg ‖
The University of Melbourne, Melbourne, Victoria 3010, Australia

This paper presents a computational fluid dynamics-driven machine learning framework to enhance Reynolds-Averaged Navier-Stokes turbulence models for complex delta wing flows at high Reynolds numbers and transonic speeds. Building upon the Coupled Spalart-Allmaras model framework, this study represents the first application of an interpretable machine learning framework to such complex three-dimensional vortex-dominated external aerodynamic applications. The key contribution lies in applying Gene Expression Programming to learn optimal anisotropy tensor corrections for delta wing flows, where the Boussinesq approximation is extended with nonlinear stress-strain terms and coupled to a redefined production term in the transport equation for turbulent viscosity. Trained on a single-delta wing configuration, the proposed approach is validated on double- and triple-delta wing geometries under challenging transonic flow conditions, demonstrating significant improvements in the prediction of aerodynamic coefficients and showcasing both accuracy and robustness. The use of Gene Expression Programming enables the automated discovery of models, generating explicit, physically interpretable expressions that provide deeper insight into vortex-dominated flow physics and facilitate generalization across related flow regimes. While the present results are specific to delta wing configurations and remain most accurate near the training conditions, they demonstrate the potential of physics-informed machine learning as a promising direction for advancing turbulence modelling in such complex three-dimensional flow regimes.

*Master of Science, Department of Aerospace Engineering, Institute of Applied Mathematics and Scientific Computing.
†Senior researcher, Department of Aerospace Engineering, Institute of Applied Mathematics and Scientific Computing.
‡Professor, Department of Aerospace Engineering, Institute of Applied Mathematics and Scientific Computing.
§This work was carried out while the author was a PhD student at the University of the Bundeswehr Munich. All data and results belong to the University of the Bundeswehr Munich. The author is currently a Postdoctoral Research Fellow at Leonardo Innovation Labs, tony.difabbio@unibw.de
¶Postdoctoral Researcher, Department of Mechanical Engineering.
‖Professor, Department of Mechanical Engineering, Lifetime Member AIAA.

Nomenclature

Abbreviations

AoA	=	Angle of attack
CSA	=	Coupled Spalart-Allmaras turbulence model
DW1	=	Triple-delta wing configuration
DW2	=	Double-delta wing configuration
EASM	=	Explicit Algebraic Stress Model
GEP	=	Gene Expression Programming
ML	=	Machine Learning
SA	=	Spalart-Allmaras turbulence model
SAnegRC	=	Spalart-Allmaras One-Equation Model with negative turbulent viscosity and Rotation/Curvature correction
VFE-2	=	Second Vortex Flow Experiment

Symbols

a_{ij}	=	extra anisotropy tensor $[Pa]$
a^*_{ij}	=	non-dimensionalized extra anisotropy tensor
c_p	=	pressure coefficient
$f^{(k)}$	=	coefficients of extra anisotropy tensor
I_k	=	scalar invariants in Pope's theory
k	=	turbulent kinetic energy $[m^2/s^2]$
Ma	=	Mach number
μ, μ_t	=	laminar and turbulent dynamic viscosity $[kg/(ms)]$
ν, ν_t	=	laminar and turbulent kinematic viscosity $[m^2/s]$
ϵ	=	turbulent dissipation rate $[m^2/s^3]$
ω	=	specific turbulent dissipation rate $[1/s]$
ρ	=	density $[kg/m^3]$
Re	=	Reynolds number
S_{ij}, W_{ij}	=	strain and rotation rate tensor $[1/s]$
S^*_{ij}	=	deviatoric strain rate tensor $[1/s]$
s_{ij}, ω_{ij}	=	non-dimensional strain and rotation rate tensor
τ_{ij}	=	Reynolds stress tensor $[Pa]$
t_l	=	turbulent time scale $[s]$
u, v, w	=	velocity vector components $[m/s]$

V_{ij}^k = extra anisotropy basis tensors

x, y, z = cartesian coordinates $[m]$

I. Introduction

Highly swept wings operating under extreme flight conditions present complex flow fields that are both challenging to predict numerically and difficult to investigate experimentally. These wings are typically utilized in agile military and supersonic aircraft due to their favorable aerodynamic performance at high Mach numbers. The aerodynamic behavior of these wings is primarily influenced by the vortex-dominated flow originating from the swept leading edge. Thus, a thorough understanding and accurate prediction of the vortical flow system are essential during the aircraft design process [1, 2]. Over the past several decades, extensive research has been conducted on the leading-edge vortices of swept wings with low aspect ratios [3–6]. In particular, Computational Fluid Dynamics (CFD) has played a central role in efforts to numerically simulate the behavior of these complex and challenging flow patterns [7–10].

Reynolds-Averaged Navier-Stokes (RANS) turbulence closure is widely preferred in industrial applications primarily because it requires significantly lower computational costs than scale-resolving simulations. Nevertheless, RANS often exhibits limited predictive accuracy when applied to complex geometries and flow dynamics, such as delta wing flows [11–16]. This limitation predominantly arises from the assumptions used in modeling the Reynolds stress tensor τ_{ij} and the turbulence model employed to close the RANS equations. A key assumption in commonly used RANS models is the Boussinesq hypothesis [17], which assumes a linear relationship between the Reynolds stress tensor and the deviatoric part of the mean strain rate S_{ij}^*. While computationally convenient, this simplification often fails to effectively capture vortical flows where stress and strain rates are misaligned or rapid redistribution of stresses occurs [18]. Several eddy-viscosity models (EVMs) have been developed, generally categorized by the number of transport equations solved to compute the eddy viscosity [19]. Among these, the Spalart-Allmaras (SA) model remains a standard choice for aerodynamic applications in the industrial sector, owing to its robustness and reliability [20]. However, the SA turbulence model shows notable discrepancies compared to the $k-\omega$ model [21], particularly in predicting delta wing flows [13, 16, 22, 23]. Therefore, both academic and industrial communities are actively investigating the sources of the inaccuracies and seeking ways to enhance the SA model's predictive capability for aerodynamic design validation in aerospace applications. To address the limitations inherent in the linear assumptions in RANS, several strategies have been proposed in the literature [16, 24–26]. Pope [27] proposed a more realistic effective-viscosity formulation, while the Quadratic Constitutive Relation (QCR) [28] supplements the linear Boussinesq approximation with a non-linear relationship between turbulent stress and strain. These approaches incorporate the anisotropic nature of Reynolds stresses, thereby addressing their previously incorrect behavior. Moreover, a previous study demonstrated that augmenting the one-equation model with an isotropic contribution of the Reynolds stress term, mathematically equivalent to introducing a fictitious turbulent kinetic energy, significantly improves the prediction of delta-wing flows at transonic conditions, thereby compensating for the absence of modeled turbulent kinetic energy [22]. Recent advances also include goal-oriented adaptive mesh refinement techniques, such as the work of Alauzet and Spalart [26], which demonstrated steady solutions for delta wing configurations at subsonic Mach numbers. Their approach highlights how mesh adaptation can effectively capture complex flow structures, complementing turbulence model corrections that mitigate excessive vortex dissipation. However, despite progress in turbulence corrections and adaptive discretization, a universally robust, broadly applicable solution to RANS turbulence-modeling limitations has yet to emerge.

Machine learning (ML) has achieved notable advancements in the domain of turbulence modeling [29]. A variety of ML techniques have been employed to improve the predictive capacity of conventional RANS models. These methodologies include calibrating model parameters via the Bayesian approach [30] and introducing a neural network-informed correction component for the turbulence production term [31], among others. More recent efforts have shifted beyond parameter tuning, aiming instead to devise new Reynolds stress closures using physics-informed machine learning. A central focus of these efforts has been refining the Boussinesq hypothesis. For example, Wang et al. [32] employed random forests to train Reynolds stress discrepancy functions. Ling et al. [33] developed a deep neural network to train the Reynolds stress tensor conserving Galilean invariance. Despite their promise, challenges persist in training and applying these models in practical engineering contexts. In particular, many of the devised corrections often lacked clear physical interpretability, and integrating the resulting neural network into standard RANS solvers presented several difficulties. A prevalent concern across many studies is the predominant focus on the so-called a-priori or frozen training techniques, wherein models are trained on static databases derived from scale-resolving data. This methodology has been adeptly executed across a plethora of ML algorithms, encompassing deep neural networks [33–36], Gaussian processes [31], random forests [32], adaptive boosting [37], sparse symbolic regression [38], and evolutionary algorithms [39]. However, the compartmentalized structure of the learning and prediction stages frequently leads to discrepancies between a-priori and a-posteriori assessments [29, 40, 41]. For this reason, several innovative approaches have emerged that integrate CFD simulations directly into the training process. Field Inversion and Machine Learning (FIML) represents a systematic framework wherein discrepancies between RANS predictions and high-fidelity data are used to infer correction fields, which are subsequently used to train machine learning models for turbulence closure enhancement [42, 43]. This approach involves "CFD-in-the-loop" training during both the field inversion and inference steps, ensuring that model corrections are directly evaluated within the CFD environment [44, 45]. Similar online training strategies have been adopted by other research groups, incorporating iterative CFD evaluations to optimize turbulence model parameters and functional forms [46, 47]. These CFD-driven frameworks, where the fitness of candidate turbulence models is directly evaluated through RANS simulations, have demonstrated significant advantages in bridging the gap between a-priori training and a-posteriori performance [47–49]. Building on the CFD-driven framework of Weatheritt and Sandberg [50] and the Coupled Spalart-Allmaras (CSA) modelling approach previously developed for wall-bounded flows [49], this study uses Gene Expression Programming (GEP) to discover interpretable turbulence model expressions for complex external aerodynamic applications. Its symbolic nature enables physically transparent modifications to the Boussinesq approximation and production terms, allowing for both model interpretability and generalizability, key advantages in extending RANS models to complex, high-Reynolds-number flows like those over delta wings.

The Vortex Flow Experiment (VFE-2) delta wing configuration is used as the training case and is investigated numerically through RANS predictions [15, 51, 52]. To reduce computational cost during the training process, calculations are performed under symmetric flow conditions (a sideslip angle of $\beta = 0°$), allowing only half of the wing to be modeled. The VFE-2 configuration features a sharp leading edge, resulting in fixed flow separation and initiating vortex formation. Consequently, the primary challenge lies in accurately modeling the formation and evolution of the vortical flow system along the wing surface. The flow field is characterized by a dominant vortex system on the suction side of the wing. At a sufficiently high angle of attack, the flow separates from the leading edge and forms one primary vortex on each half. The vortex is continuously fed by the separation over the whole length of the leading edge [51]. A secondary vortex, rotating in the opposite direction, forms between the wing surface and the primary vortex, drawing energy predominantly from the latter. At higher angles of attack, this secondary vortex breaks down, which in turn disrupts the shear layer roll-up and potentially triggers the breakdown of the primary vortex. This leads to significant changes in the downstream flow field [15]. Since conventional EVMs often fail to replicate these flows with vortex breakdown [14, 15], new turbulence models are assessed. The CFD-driven GEP training aims to improve the performance of the one-equation turbulence model by integrating two key strategies: (i) extending the linear Boussinesq hypothesis to capture Reynolds stress anisotropy better, and (ii) enhancing the modeling of turbulence production and dissipation in delta wing flows. Extending the CSA model framework to vortex-dominated external aerodynamics, we employ a model in which the production term incorporates a nonlinear extension of the Boussinesq approximation. GEP is then used to discover an improved anisotropic tensor a^*_{ij}, which both extends the Boussinesq model and modifies the production term in the $\tilde{\nu}$ transport equation. This enables joint optimization of Reynolds stress representation and turbulence production, forming the core of the modeling framework. RANS model training is conducted at two angles of attack (AoA, α): $\alpha = 20.5°$, where experimental data indicate the absence of primary vortex breakdown, and $\alpha = 25.6°$, where breakdown of the primary vortex is observed. Both simulations are conducted at a Mach number of 0.80 and a Reynolds number of 2×10^6, using reference experimental data from the German Aerospace Center (DLR) [51]. The turbulence models obtained with the CFD-driven GEP training are then validated on two additional configurations: the DW1 (triple-delta wing) and DW2 (double-delta wing) [53]. Multiple-swept wing configurations are analyzed under transonic conditions with a $Ma = 0.85$ and a $\mathrm{Re} = 12.53 \times 10^6$. The configurations are tested at $\alpha = 12°$, $16°$, $20°$, $24°$, and $28°$ under asymmetric flow conditions, with $\beta = 5°$, featuring aerodynamic characteristics with notable differences [22, 54]. This validation represents a significant extrapolation test, as the models trained under symmetric conditions ($\beta = 0°$) are evaluated under asymmetric flow conditions with $\beta = 5°$, requiring the prediction of complex three-dimensional aerodynamic phenomena that were not present during training. The proposed turbulence model modifications achieve a certain degree of generalizability, highlighting the broader applicability of genetic algorithms in advancing the field of turbulence modeling. This work marks the first application of the CFD-driven GEP framework to complex three-dimensional external aerodynamic problems at transonic speeds and high Reynolds numbers, thereby extending machine learning-based turbulence modeling from wall-bounded flows to highly challenging, vortex-dominated industrial applications. The results highlight the potential of data-driven approaches in advancing predictive accuracy and robustness of RANS models for aerospace engineering applications.

The structure of this paper is organized as follows. Section II outlines the methodology employed for improving the accuracy of RANS calculations. Section III describes the test cases, detailing the computational domain and the numerical setup.Section IV presents the CFD results, with Section IV.A focusing on the training outcomes for the VFE-2 configuration, and Section IV.B discussing the validation results for additional configurations. Finally, Section V summarizes the key findings and conclusions of the study.

II. Methodology

The two integrated methodologies are presented in this section. The first component of the methodology focuses on extending the Boussinesq hypothesis to account for the anisotropy of the Reynolds stress tensor, as detailed in Section II.A. The second involves the integration of this anisotropy correction into the CSA model's production term, forming a novel one-equation turbulence model, described in Section II.B. The training of this coupled model using the GEP framework, aimed at optimizing both anisotropy modeling and turbulence production, is presented in Section II.C. Additional methodological details can be found in the authors' previous publication [49].

A. The modeling of the Reynolds stress anisotropy

The RANS equations are derived from the Navier-Stokes equations by decomposing the flow field into mean and fluctuating components, where the latter accounts for turbulence effects. For a compressible Newtonian fluid, the Favre-averaged RANS momentum equations using Einstein summation convention are given by

$$\frac{\partial(\bar{\rho}\tilde{u}_i)}{\partial t} + \frac{\partial(\bar{\rho}\tilde{u}_i\tilde{u}_j)}{\partial x_j} = \bar{\rho}\tilde{f}_i + \frac{\partial}{\partial x_j}\left[-\bar{p}\delta_{ij} + \tilde{\tau}_{ij} - \overline{\rho u_i'' u_j''}\right], \tag{1}$$

where the overbar ($\bar{}$) denotes Reynolds averaging, the tilde ($\tilde{}$) denotes Favre (density-weighted) averaging defined as $\tilde{\phi} = \overline{\rho\phi}/\bar{\rho}$, and double primes ($''$) represent Favre fluctuations defined as $\phi'' = \phi - \tilde{\phi}$. The viscous stress tensor is given by

$$\tilde{\tau}_{ij} = \tilde{\mu}\left(\frac{\partial\tilde{u}_i}{\partial x_j} + \frac{\partial\tilde{u}_j}{\partial x_i} - \frac{2}{3}\frac{\partial\tilde{u}_k}{\partial x_k}\delta_{ij}\right) \tag{2}$$

The left-hand side represents the unsteady and convective transport of mean momentum, while the right-hand side includes contributions from body forces, mean pressure, viscous stresses, and the Reynolds stress tensor $-\overline{\rho u_i'' u_j''}$, which arises from velocity fluctuations. Due to the non-linear convective term, turbulence models are required to achieve closure. The Boussinesq hypothesis approximates the Reynolds stress tensor as proportional to the traceless mean strain rate tensor $\tilde{S_{ij}^*}$, expressed as

$$-\overline{\rho u_i'' u_j''} = \tau_{ij} = 2\mu_t \tilde{S_{ij}^*} - \frac{2}{3}\bar{\rho}\tilde{k}\delta_{ij} \tag{3}$$

where μ_t is the turbulent (eddy) viscosity, $\tilde{k} = \frac{1}{2}\widetilde{u_i'' u_i''}$ is the turbulent kinetic energy, and $\tilde{S_{ij}^*}$ is the traceless mean strain rate tensor defined as

$$\tilde{S_{ij}^*} = \tilde{S_{ij}} - \frac{1}{3}\tilde{S_{kk}}\delta_{ij} = \frac{1}{2}\left(\frac{\partial \tilde{u}_i}{\partial x_j} + \frac{\partial \tilde{u}_j}{\partial x_i}\right) - \frac{1}{3}\frac{\partial \tilde{u}_k}{\partial x_k}\delta_{ij}. \tag{4}$$

Turbulence closures resembling Explicit Algebraic Stress Models (EASMs) improve upon the limitations of the Boussinesq hypothesis by incorporating an additional anisotropic stress term, a_{ij}, into the Reynolds stress tensor equation:

$$-\tau_{ij} = \frac{2}{3}\bar{\rho}\tilde{k}\delta_{ij} - 2\mu_t \tilde{S_{ij}^*} + 2\rho k a_{ij}. \tag{5}$$

EASM-like closures can be generally expressed in a non-dimensionalized form:

$$a_{ij}^* = \sum_k f^{(k)}(I_1, I_2, ..., I_n)V_{ij}^k, \tag{6}$$

where a_{ij}^* is constructed using the basis tensors V_{ij}^k and scalar invariants I_k. The coefficients $f^{(k)}$ are determined via symbolic regression using GEP [50]. Three basis tensors and two invariants, written in Eq. 7, are used to reduce complexity [49, 55], and the results show the appropriateness of this choice.

$$V_{ij}^1 = s_{ij}, \quad V_{ij}^2 = s_{ik}\omega_{kj} - \omega_{ik}s_{kj}, \quad V_{ij}^3 = s_{ik}s_{kj} - \frac{1}{3}\delta_{ij}s_{mn}s_{mn}, \quad I_1 = s_{mn}s_{nm}, \quad I_2 = \omega_{mn}\omega_{nm}. \tag{7}$$

Therefore, V_{ij}^k and I_k are expressed based on the non-dimensionalized strain rate tensor, $s_{ij} = t_l\tilde{S_{ij}^*}$, and rotation rate tensor, $\omega_{ij} = t_l\tilde{W_{ij}}$, where $\tilde{W_{ij}}$ represents the vorticity tensor. Inspired by the SA-QCR model [28], the turbulence time scale t_l is formulated as

$$t_l = \frac{1}{\sqrt{\frac{\partial u_m}{\partial x_n}\frac{\partial u_m}{\partial x_n}}} \quad \text{where} \quad \sqrt{\frac{\partial u_m}{\partial x_n}\frac{\partial u_m}{\partial x_n}} = \sqrt{u_x^2 + u_y^2 + u_z^2 + v_x^2 + v_y^2 + v_z^2 + w_x^2 + w_y^2 + w_z^2}. \tag{8}$$

The dimensionalized anisotropic stress tensor a_{ij} is obtained from the non-dimensionalized a^*_{ij} as follows

$$a_{ij} = \frac{2\mu_t a^*_{ij}}{t_l}. \tag{9}$$

Thus, the modified Reynolds stress tensor equation is expressed as

$$-\tau_{ij} = \frac{2}{3}\bar{\rho}\tilde{k}\delta_{ij} - 2\mu_t \tilde{S^*_{ij}} + \frac{2\mu_t a^*_{ij}}{t_l} = \frac{2}{3}\bar{\rho}\tilde{k}\delta_{ij} - 2\mu_t\left(\tilde{S^*_{ij}} - \frac{a^*_{ij}}{t_l}\right). \tag{10}$$

B. The Coupled Spalart-Allmaras turbulence model

The development of the CSA turbulence model [49] builds upon the well-established two-equation $k-\omega$ model by Wilcox [19]. To modulate the destruction term, a blending function f_d is introduced, following hybrid RANS/LES approaches [56]. This function enables a smooth transition between near-wall and off-wall regions, effectively mitigating excessive dissipation near solid boundaries. The modified destruction term retains consistency with the original SA model while improving predictions in high-strain-rate regions. The complete derivation is available in [49]. The transport equation for the CSA model is formulated as follows

$$\frac{D\tilde{\nu}}{Dt} = 2c_{b1}t_l S^*_{ij}\frac{\partial u_i}{\partial x_j}\tilde{\nu} - c_{w1}f_w\tilde{D}\tilde{\nu} + \frac{1}{\sigma}\left[\frac{\partial}{\partial x_j}\left((\nu+\tilde{\nu})\frac{\partial\tilde{\nu}}{\partial x_j}\right) + c_{b2}\frac{\partial\tilde{\nu}}{\partial x_i}\frac{\partial\tilde{\nu}}{\partial x_i}\right], \tag{11}$$

where the destruction term depends on the parameter

$$\tilde{D} = \frac{\tilde{\nu}}{d^2} - f_d\cdot\min\left(\frac{\tilde{\nu}}{d^2} - \sqrt{\beta^*}|S_{ij}|^2 t_l, 0\right). \tag{12}$$

Here, $\beta^* = 0.09$ from [19] and $|S_{ij}| = \sqrt{2S_{ij}S_{ij}}$ is the magnitude of the strain rate tensor. Moreover, in the turbulence model denoted as CSA+a_{ij}, the modeled anisotropic stress tensor a_{ij} is incorporated directly into the turbulence production term, allowing simultaneous optimization of both anisotropy modeling and turbulence production. The production term (i.e., first term on the right-hand side of Eq. 11) is modified as follows

$$P = 2c_{b1}\left(S^*_{ij}t_l - a^*_{ij}\right)\frac{\partial u_i}{\partial x_j}\tilde{\nu}. \tag{13}$$

The new production term has the advantage that changes in τ_{ij} are reflected as well in P, not just in the Boussinesq assumption. In this way, a twofold optimization is possible while modeling the anisotropy of the Reynolds stress. In a previous study [49], we demonstrated that the coupling in the CSA+a_{ij} model is essential for enhancing one-equation turbulence modeling, as it significantly improves predictive accuracy across various flow configurations. The ML-GEP objective is to discover an improved anisotropic stress tensor a^*_{ij}, which not only extends the Boussinesq approximation for Reynolds stress anisotropy but also modifies the turbulence production term in the $\tilde{\nu}$ transport equation, as shown in Eq. 13. The simultaneous influence of a^*_{ij} on both the stress representation and production dynamics is a key element of this modeling approach.

C. Training frameworks: CFD-driven method

The study integrates CFD simulations into model training, termed CFD-driven training [47, 48], as illustrated in Fig. 1. This framework consists of two core components: a CFD solver, using the DLR TAU-Code [57] for RANS computations, and an ML module employing GEP due to its demonstrated effectiveness in turbulence closure modeling [47, 48, 58, 59]. In every iteration, candidate expressions generated by GEP are integrated by TAU, and the RANS calculations are subsequently performed. Model performance is evaluated by the cost functions that compute the discrepancy between RANS results and the reference data. At this point, GEP reads the cost function values to guide the evolutionary process, generating new candidate expressions that aim to minimize the mean square deviation between numerical and experimental results. The methodology was originally introduced by Weatheritt and Sandberg [50] for turbulence modeling. The training begins with randomly initialized EASMs, where the tensor bases V^k_{ij} remain fixed, and the coefficients $f^{(k)}$ are optimized. For the hyperparameter setup, each model consists of 4 genes, with expression trees constrained by a head length of 5 and a maximum tree size of 12. The population size is set to 400, evolving over 100 generations [50, 60]. The CSA+a_{ij} turbulence equation is employed to optimize Reynolds stresses and production term, consistent with previous studies [48, 50]. For the training computational cost, 2875 RANS calculations had to be executed (25 per generation after the initial population assessment), each requiring 35 – 55 minutes on 48 cores.

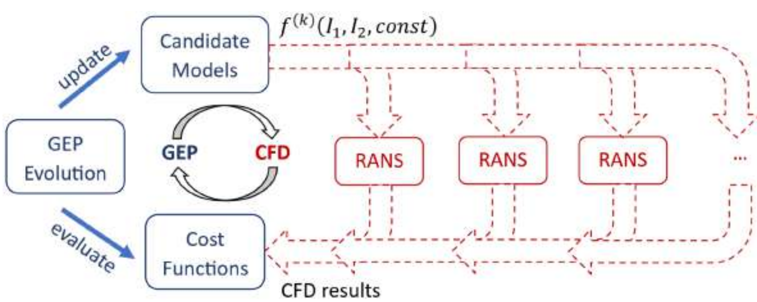

Fig. 1 CFD-driven training scheme [48].

In the present study, the pressure coefficient distribution along the VFE-2 wing's surface at five locations is used to define the cost functions. These locations, denoted by $\xi = 0.2, 0.4, 0.6, 0.8, 0.95$ as shown in Fig. 2, are selected to capture the spatial evolution of the vortical flow. The pressure coefficient is a key indicator for identifying vortex structures, as it reflects the suction imprint on the upper wing surface in terms of both location and magnitude. Therefore, an accurate prediction of the negative pressure field is considered indicative of correctly capturing the underlying flow phenomena.

A multi-objective training is performed, where each of the five locations is trained as a separate objective within the optimization process. This enables the GEP framework to minimize the five deviations simultaneously. To assess the performance of each candidate model, the non-dimensionalized mean square error between numerical and experimental data is computed as

$$\Phi = \frac{1}{N} \sum_{i=1}^{N} \left(\frac{C_{p,\mathrm{RANS}}(y_i) - C_{p,\mathrm{Exp}}(y_i)}{\max(C_{p,\mathrm{Exp}})} \right)^2, \qquad (14)$$

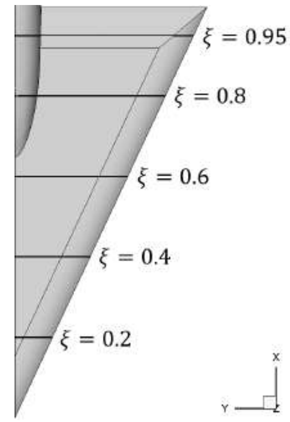

Fig. 2 Probing location on the VFE-2.

where the subscripts 'Exp' and 'RANS' denote experimental data and numerical predictions, respectively. The deviation $C_{p,\mathrm{RANS}} - C_{p,\mathrm{Exp}}$ is computed at discrete y-locations, summed, and normalized by $\max(C_{p,\mathrm{Exp}})$. The baseline model provides accurate predictions, resulting in low values of the cost function Φ at $\xi = 0.2$ and $\xi = 0.4$, whereas larger discrepancies appear at the remaining locations. To improve model sensitivity in the regions of poor performance, the fitness values at $\xi = 0.6, 0.8, 0.95$ were normalized by the baseline costs. This ensures that models performing poorly at the three locations incur higher penalties while improved models receive lower costs. Since further refinements at $\xi = 0.2$ and $\xi = 0.4$ are limited, normalizing the already low costs could mislead optimization priorities and is therefore avoided. The overall fitness of each model is then determined as the weighted average of the costs at all probe locations.

III. Test Cases and Numerical Approach

The VFE-2 test case is introduced in Section III.A, while the DW1 and DW2 multiple-delta wings are presented in Section III.B. Section III.C details the numerical approach employed within the DLR TAU-Code.

A. Training Case and Mesh Convergence Study

The VFE-2 delta wing illustrated in Fig. 3 features a 65° sweep angle [52, 61]. Given its root chord length of 0.980 m, it possesses a span of 0.914 m and covers an area of 0.448 m^2. It has a thickness of 0.033 m. The wing's aspect ratio stands at 1.86. Dimensionless Cartesian coordinates are introduced as follows: $\xi = x/L$, $\eta = y/(x \cdot tan(\phi))$ and $\psi = z/(x \cdot tan(\phi))$, where L is the characteristic length, here chosen as the chord length in the symmetry plane. Training is performed at $Ma = 0.80$ and Re $= 2 \times 10^6$, separately at $\alpha = 20.5°$ and $\alpha = 25.6°$. To manage computational costs, a mesh convergence study has been conducted to identify a grid resolution that is coarse enough to conduct thousands of simulations while still ensuring a sufficient level of accuracy. This study is performed at $\alpha = 25.6°$, where the primary vortex breakdown occurs. The results are presented in Fig. 4.

The selection of the "2M" mesh is justified by first examining the region at $\xi = 0.2$, near the leading-edge apex, where achieving mesh convergence is particularly challenging due to the onset of flow separation and vortex formation. Although this region is highly sensitive to mesh resolution, the deviations observed in the "2M" results remain within an acceptable range for the study's objectives. Furthermore, at $\xi = 0.6$, significant discrepancies are observed in the "1M" mesh results compared to the "10M" mesh, indicating insufficient spatial resolution. These observations further validate the "2M" mesh as a practical compromise between accuracy and computational cost.

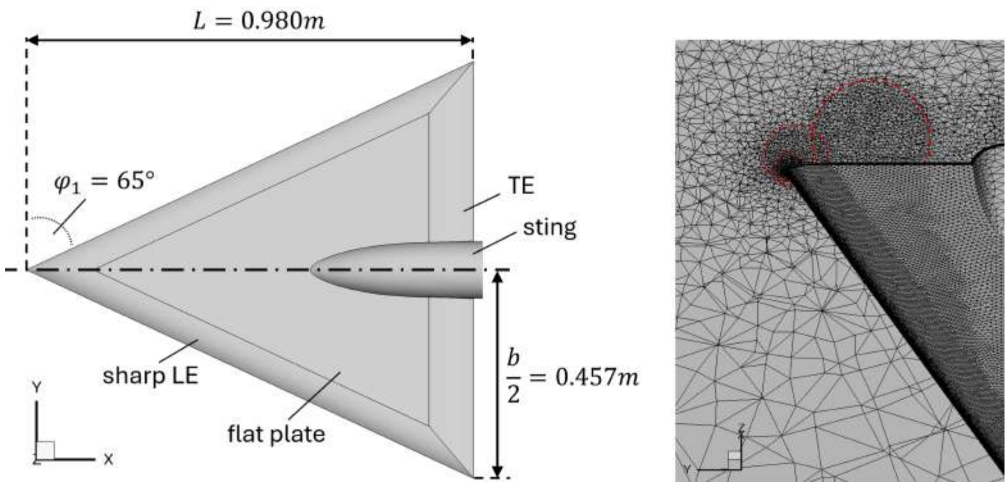

Fig. 3 VFE-2 geometry and mesh. LE and TE refer to the leading and trailing edge, respectively.

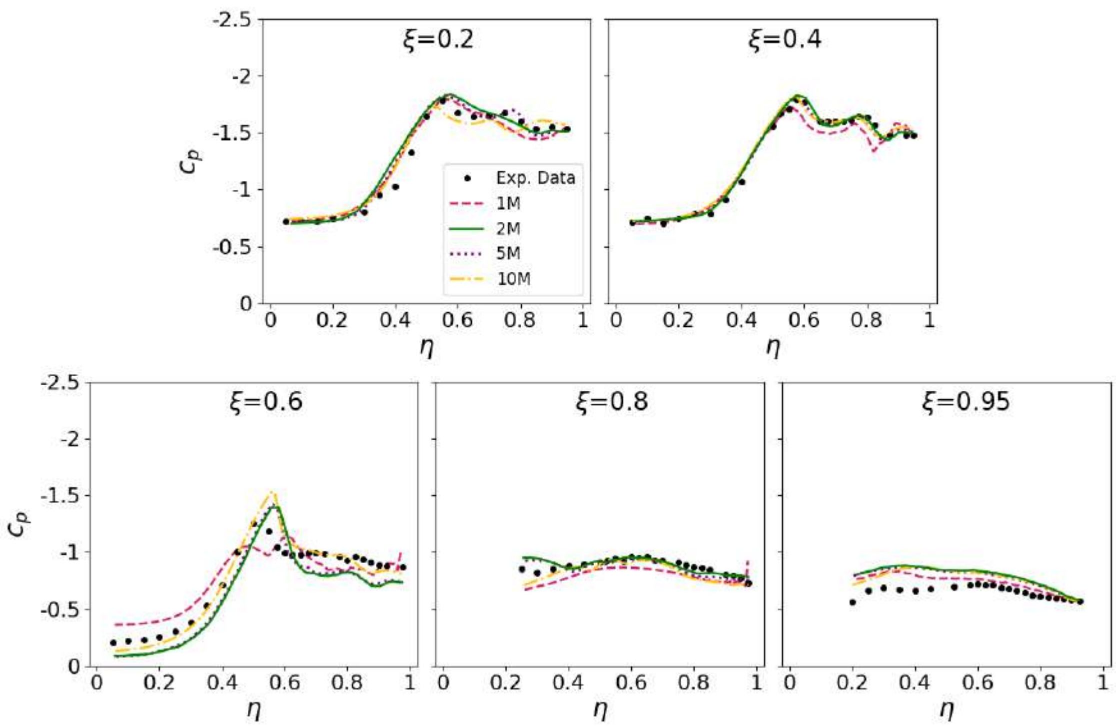

Fig. 4 VFE-2 mesh convergence study at $\alpha = 25.6°$**,** $Ma = 0.8$**, and** $\mathrm{Re} = 2 \times 10^6$**.**

The chosen mesh comprises approximately 2 million grid points and includes 25 prism layers near the wing surface. The first cell layer height is determined to satisfy $y^+ \approx 1$, with subsequent layers growing by a height ratio of 1.2 in the wall-normal direction. Polyhedral volumes are used throughout the mesh. The cell's size varies within the computational domain, with higher resolution concentrated around and on top of the wing. Particular attention is directed towards the leading and trailing edges. The sharp leading edge is subtly rounded to ensure superior mesh quality with well-defined surface normals surrounding the edge. The finest cells are located near the leading edge to resolve the onset of the shear layer and to capture the development of turbulent scales within the vortex region. The outer boundary is formed by a spherical farfield boundary located $50L$ from the wing to eliminate any non-physical effects on the solution due to numerical boundary conditions applied at the farfield.

B. Validation Cases

The DW1 configuration shown in Fig. 5a features a triple-delta wing. A mid-wing strake follows with an increased sweep of $\phi_2 = 75°$, and the rear wing section transitions back to a sweep of $\phi_3 = 52.5°$. The rear section has the largest surface area with a reference area of $A_{\text{ref}} = 0.082236\,\text{m}^2$, a root chord length of $c = 0.58\,\text{m}$ and a wing half-span of $b = 0.4166\,\text{m}$. The mesh for DW1 is described in detail in Di Fabbio et al. [14]. The DW2 configuration shown in Fig. 5b features a double-delta wing and is more slender than DW1. A strake with a sweep angle of $\phi_1 = 75°$ branches from the fuselage, transitioning into a larger wing area with a sweep angle of $\phi_2 = 52.5°$. The characteristic length remains $c = 0.580\,\text{m}$, but increased slenderness results in a reduced wing span of $b = 0.3664\,\text{m}$ and a smaller reference area of $A_{\text{ref}} = 0.06688\,\text{m}^2$. Details for the DW2 mesh can be found in Rajkumar et al. [54]. Appropriate mesh convergence studies are reported in the references mentioned before [14, 54].

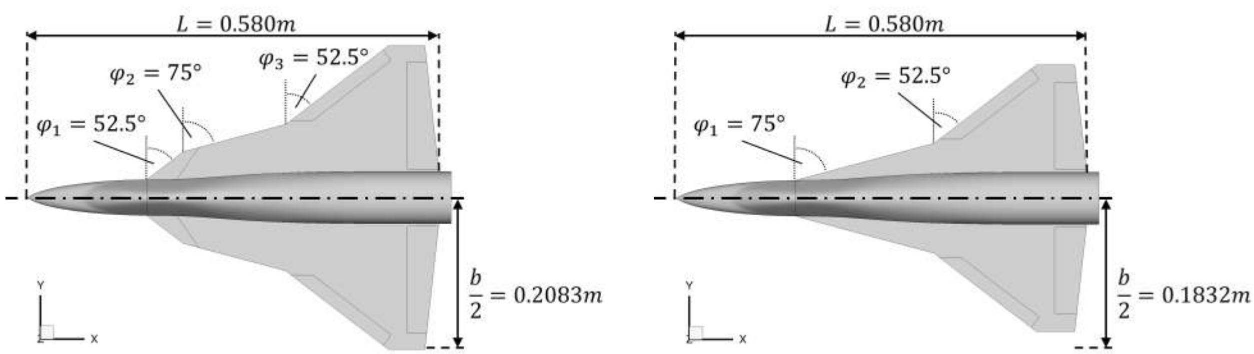

(a) The DW1 triple-delta wing. **(b) The DW2 double-delta wing.**

Fig. 5 Validation case geometries.

Validation cases for the DW1 and DW2 configurations are conducted under significantly different conditions than those used during training. Notably, while training was performed under symmetric flow conditions ($\beta = 0°$), the validation cases operate under asymmetric flow conditions with a sideslip angle of $\beta = 5°$. This represents a substantial extrapolation challenge, as the models must predict complex three-dimensional flow interactions, including non-zero roll moments, without prior exposure to such asymmetric conditions during training. Additionally, the validation is conducted at transonic conditions with $Ma = 0.85$ and $\mathrm{Re} = 12.53 \times 10^6$. The configurations are analyzed at $\alpha = 12°, 16°, 20°, 24°$, and $28°$ because the flow behavior and aerodynamic characteristics exhibit notable differences for the different AoA [14, 22, 54].

C. Numerical Approach

RANS calculations are performed using the DLR TAU-Code [57], a compressible CFD solver. Initially, for the initialization of the simulations, an upwind scheme is used in combination with the implicit Euler method and the Lower-Upper Symmetric Gauss-Seidel (LUSGS) scheme. Stepwise, the CFL number and the order of the upwind flux are increased to stabilize the simulation. After initialization, a central scheme with matrix dissipation is employed to compute the mean fluxes. To smooth the results of the genetically optimized models for post-processing, an additional step is introduced to perform unsteady simulations (URANS) using dual-time stepping, employing a Backward-Euler/LUSGS implicit smoother. The time step size equals 1×10^{-4} s. Ten CTUs are computed before starting the time-averaging to overcome the initial transient, and five flow-through times are considered in the computation of the mean flow field values. The matrix dissipation model is selected while computing the fluxes with a central scheme [62].

For training, each simulation begins from an already converged baseline solution. A fixed maximum of 5000 iterations is executed using the central scheme in combination with matrix dissipation. This is because candidate models derived from GEP may exhibit different convergence behavior with an unknown number of required iterations to reach convergence, as well as an unknown threshold for a converged solution. Using 5000 iterations ensures sufficient time for the initial rise in residuals to decay, allowing the models to reach a converged state.

IV. Results and discussion

The CFD results are presented in the following sections. The training outcomes for the VFE-2 configuration are shown in Section IV.A, while the multi-swept wing validation results are discussed in Section IV.B.

A. CFD-driven training outcomes: the importance of the selected flow conditions.

Training results are first presented for the lower AoA of 20.5° before proceeding with the results at a higher incidence angle of 25.6°. Separate turbulence models are trained for each angle of attack, as indicated with the appendices 20 and 25, respectively. The results are presented independently for each angle of attack to evaluate model performance across different flow conditions while maintaining the same geometry. Therefore, the influence of flight conditions on training is discussed, highlighting the models' applicability and generalizability. These aspects will be further illustrated through the validation results for the DW1 and DW2 configurations. The spanwise distribution of the pressure coefficient at each probe location, as marked in Fig. 2, is evaluated to assess the performance of the genetically optimized models relative to their counterparts. The distribution of c_p on the wing's upper surface is also examined to provide insight into the size, magnitude, and location of the suction imprint induced by the vortex system. A comparison of the GEP expressions obtained from training both genetically optimized turbulence models is also discussed. The methodologies presented in Section II are applied, and four simulation results are compared with the experimental data.

1) SAnegRC: Spalart-Allmaras One-Equation Model with negative turbulent viscosity and Rotation/Curvature correction [20, 63] and applying the Boussinesq assumption in Eq. 3. This constitutes the baseline model.
2) CSA: The new one-equation turbulence model in Eq. 11 and applying the Boussinesq assumption. The CSA baseline model is included in the discussion to provide a well-defined starting point for the analysis, establishing a clear reference for comparison and justifying the improvements introduced by the more advanced models presented in this paper.

3-4) CSA+a_{ij}: The modeled a_{ij} is included in the new turbulence production term in Eq. 13. This allows for optimization of both the anisotropy tensor and the turbulence production term with the same three coefficients: $f^{(1)}$, $f^{(2)}$, and $f^{(3)}$ (as detailed in Section II.C). The training is performed at two angles of attack, 20.5° and 25.6°, resulting in different nomenclature for the presentation of the results: CSA+a_{ij}_20 and CSA+a_{ij}_25, respectively.

1. Absence of the vortex breakdown: AoA = 20.5°

The spanwise distribution of the pressure coefficient at different locations for an AoA of 20.5° is illustrated in Fig. 6. At $\xi = 0.2$, near the wing apex, no significant differences between the considered turbulence models are observed. Further downstream, at $\xi = 0.4$, only the genetically optimized models correctly capture the magnitude and location of the peak in the negative pressure coefficient at $\eta \approx 0.6$ of the primary vortex. The CSA+a_{ij} models predict the presence of a secondary vortex at $\eta \approx 0.78$, slightly more pronounced for CSA+a_{ij}_25, which is found to be weaker in the experiments. The baseline CSA model fails to capture the plateau in the pressure coefficient around $\eta \approx 0.70$, potentially indicating a wider vortex or a denser vortex system, which does not distinguish between the primary and secondary vortices. Apart from these exceptions, all other models follow the trend of the experimental data but tend to predict a stronger suction peak, shifted further outboard.

Significant differences between turbulence models appear at $\xi = 0.6$. All models correctly predict the primary vortex location and magnitude. However, a weak secondary vortex is observed in the experimental data at $\eta = 0.82$, and the outcomes differ in their accuracy in predicting this phenomenon. CSA and CSA+a_{ij}_25 overpredict the magnitude and size of the secondary vortex. SAnegRC and CSA best distinguish between the primary and secondary vortices by achieving lower c_p levels between the peaks around $\eta \approx 0.71$. At $\xi = 0.8$, all models except CSA+a_{ij}_20 overpredict the pressure coefficient along the wingspan. At the final location, $\xi = 0.95$, CSA and SAnegRC behave similarly. Near the leading edge, up to $\eta \approx 0.6$, CSA+a_{ij}_25 provides the most accurate pressure coefficient predictions among all turbulence models. Further outboard, CSA+a_{ij}_25 deviates from the experimental data, reaching $c_p \approx -0.7$, a value that other models come at the plateau between $0.57 \leq \eta \leq 0.8$. The CSA+a_{ij}_20 model, trained explicitly for this AoA, does not reach this c_p level in the given range, highlighting the challenges of predicting all the relevant phenomena over the wing. At this location, both the CSA+a_{ij} models accurately predict the negative c_p peak, indicating a weaker primary vortex presence at the rear wing, as confirmed by the experimental data.

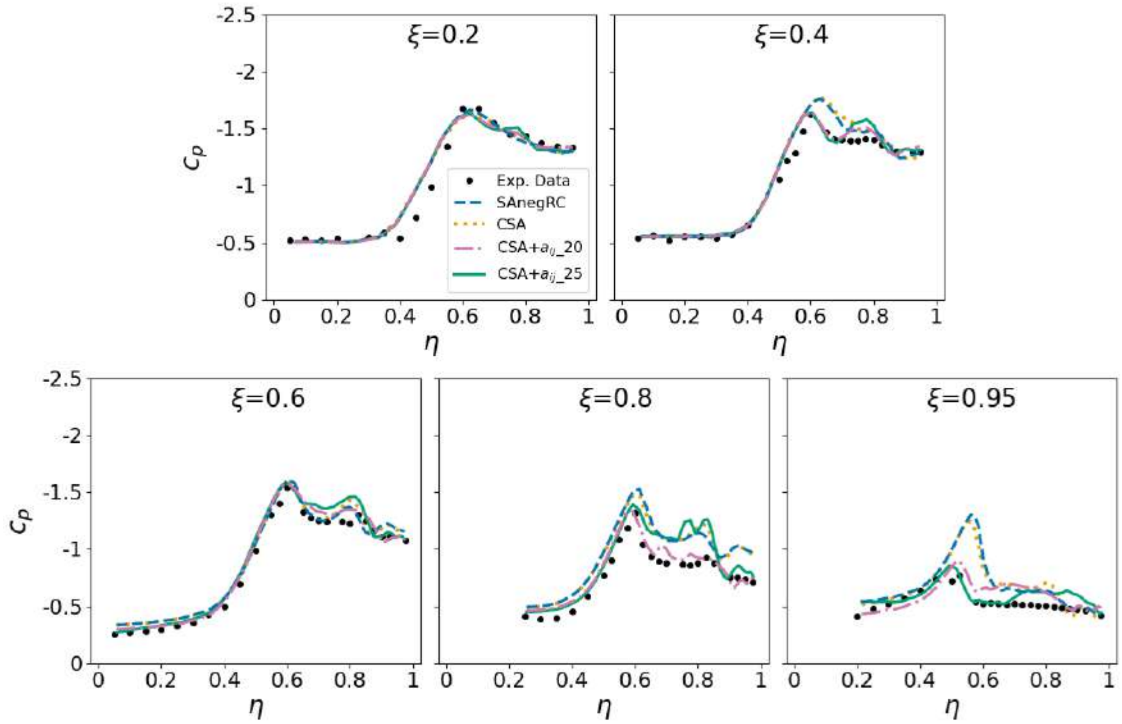

Fig. 6 Spanwise pressure coefficient distribution at $\alpha = 20.5°$**.**

The CSA+a_{ij}_25 model, trained at a higher AoA, accurately captures the behavior of the primary vortex along the entire wing. However, it exhibits discrepancies in predicting secondary and related phenomena, particularly those that develop between the primary vortex and the leading edge. In contrast, these discrepancies disappear when in the CSA+a_{ij}_20 model, which was trained explicitly for this angle of incidence and therefore provides the best overall agreement with the experimental data.

2. Prediction of the vortex breakdown: AoA = 25.6°

At an AoA of 25.6°, the regime corresponds to a condition where the breakdown of the primary vortex is observed, and vortices are no longer present downstream of $\xi = 0.8$, as illustrated in Fig. 7. At $\xi = 0.2$ and $\xi = 0.4$, no model significantly deviates from the predicted pressure coefficient. However, at $\xi = 0.6$, notable differences arise between the considered models. While SAnegRC predicts the location and magnitude of the peak negative pressure with varying degrees of accuracy, it generally underpredicts the overall magnitude of the pressure coefficient near the leading edge. In contrast, the CSA and CSA+a_{ij}_20 models exhibit a noticeable overprediction of the suction footprint and indicate the presence of a secondary vortex at $\xi \approx 0.8$. The CSA+a_{ij}_25 model is the only model that accurately reproduces the experimental data and therefore provides the most accurate prediction of the primary vortex and its subsequent breakdown.

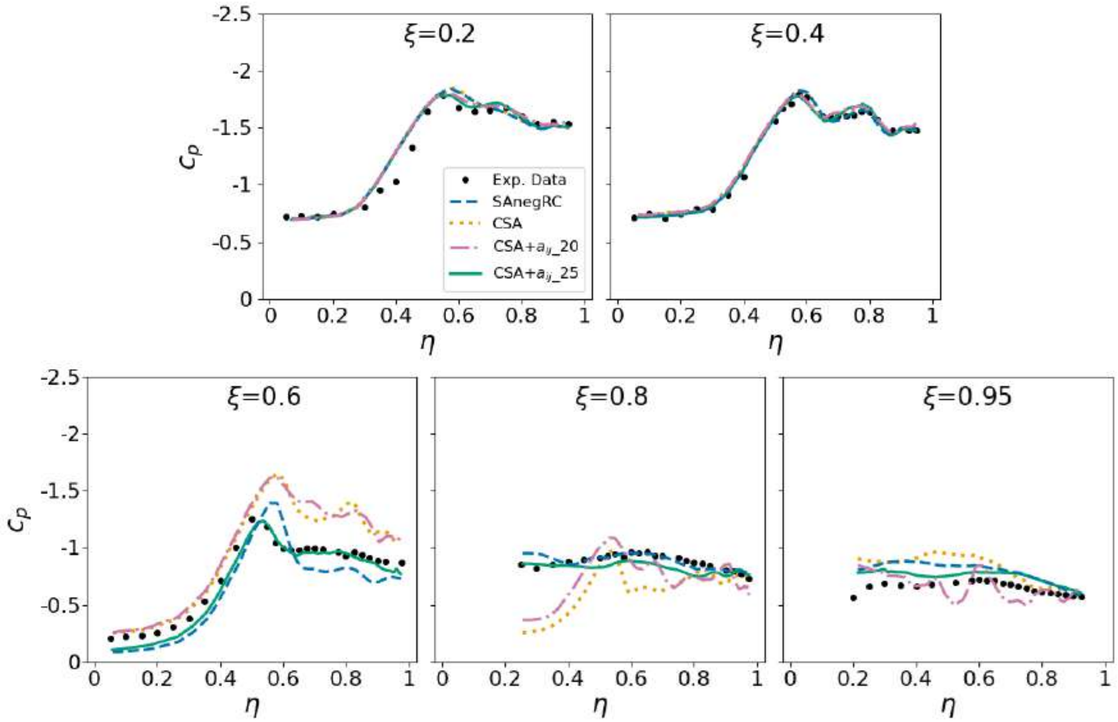

Fig. 7 Spanwise pressure coefficient distribution at $\alpha = 25.6°$**.**

At $\xi = 0.8$, CSA and CSA+a_{ij}_20, which previously overpredicted the suction footprint at $\xi = 0.6$, fail to predict the collapse of the vortex system and still indicate the presence of vortices. This analysis highlights the critical role of the secondary vortex in influencing the vortex system. As demonstrated in a previous author's work [15, 22], the breakdown of the primary vortex is linked to the earlier breakdown of the secondary vortex, which disrupts the shear layer and prevents vorticity feeding. This loss of kinetic energy renders the primary vortex susceptible to breakdown. Moreover, at $\xi = 0.8$ and $\xi = 0.95$, CSA+a_{ij}_20 exhibits instabilities and fluctuations in the predicted pressure coefficient. These fluctuations are difficult to attribute to any evident physical phenomenon, suggesting that incoherent structures may also occur upstream of the vortex breakdown at this angle of attack. CSA+a_{ij}_25 predicts a slightly higher pressure coefficient than observed in the experiments; however, its results remain satisfactorily accurate compared to other models and experimental data. At $\xi = 0.95$, all models except for CSA+a_{ij}_20 correctly predict the absence of vortices in the rear region. Overall, CSA+a_{ij}_25 provides the most accurate predictions, confirming the importance of flow conditions in the training process.

3. Comparison of the genetically optimized models

Following the previous performance analysis, the genetically optimized models CSA+a_{ij}_20 and CSA+a_{ij}_25 are further assessed. In Fig. 8, the evolution of the cost function, specifically the weighted average of the non-dimensionalized mean square error Φ (see Eq. 14), is plotted over 50 generations. Notably, with the initialization of the population, the cost function improves for both AoA. While the cost for $\alpha = 25.6°$ progressively decreases over multiple generations until approximately generation 25, the CSA+a_{ij} models for $\alpha = 20.5°$ exhibit significant improvement primarily within the first five generations. Finally, the cost function at $\alpha = 20.5°$ consistently achieves the lowest cost among both models. For the critical location $\xi = 0.6$, the cost function values are mentioned explicitly. At $\alpha = 20.5°$, the true average cost of CSA+a_{ij}_20 is $\Phi_{0.6} = 0.0306$, representing an improvement of over 77% compared to the CSA baseline model, which has a cost of $\Phi_{\mathrm{base},0.6} = 0.1339$ at the same AoA. At $\alpha = 25.6°$, the true average cost of CSA+a_{ij}_25 is $\Phi_{0.6} = 0.0407$, compared to $\Phi_{\mathrm{base},0.6} = 0.3766$ for the CSA baseline model, indicating an improvement of over 89%. These results confirm that both optimized models significantly outperform the baseline model in terms of the cost function Φ. The CSA formulation, therefore, holds great potential for one-equation turbulence model enhancement.

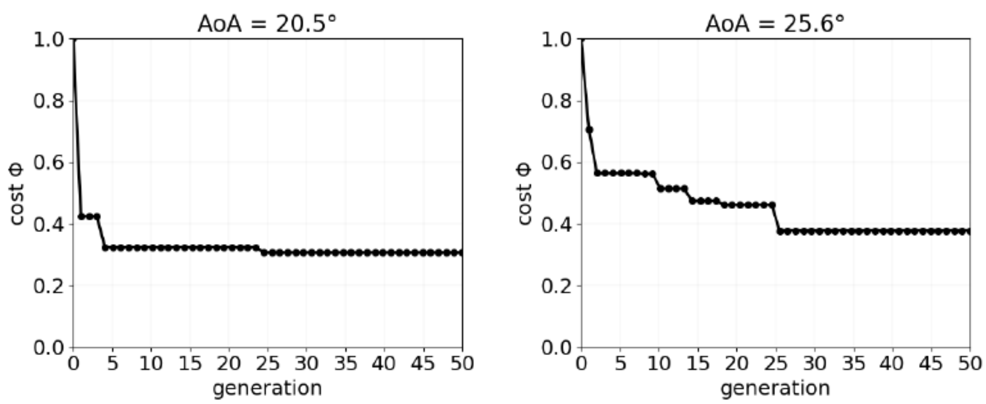

Fig. 8 Evolution of the weighted-average cost function Φ.

The corresponding expressions for the coefficients of the basis tensors obtained from the GEP optimization are summarized in Table 1. Both models employ a linear formulation for two scalars and a more complex formulation for the remaining scalar. However, the complexity of the formulation is not associated with the same scalar in both cases. The linear formulations in CSA+a_{ij}_25 involve both invariants and a constant, whereas in CSA+a_{ij}_20, they are based on either the first or second invariant and constants. To visualize their dependencies, the scalars $f^{(1)}$, $f^{(2)}$ and $f^{(3)}$ are plotted in Fig. 9 as functions of the normalized invariants I_1^* and I_2^*, which correspond to the invariants I_1 and I_2 normalized by their respective maximum values, $I_{1,\max}$ and $I_{2,\max}$.

AoA	20.5°	25.6°
$f^{(1)}$	$0.15(1.097I_2 - 0.008)(-2I_1 + I_2 + 0.43)$	$I_1 - I_2 + 0.4945$
$f^{(2)}$	$-2.795I_1 - 4.266$	$I_1 + I_2 + 0.641$
$f^{(3)}$	$-0.58I_2 - 0.061$	$-0.00645(I_1^3 - 0.03075)$

Table 1 Expressions obtained from GEP for CSA+a_{ij} at $\alpha = 20.5°$ and $25.6°$.

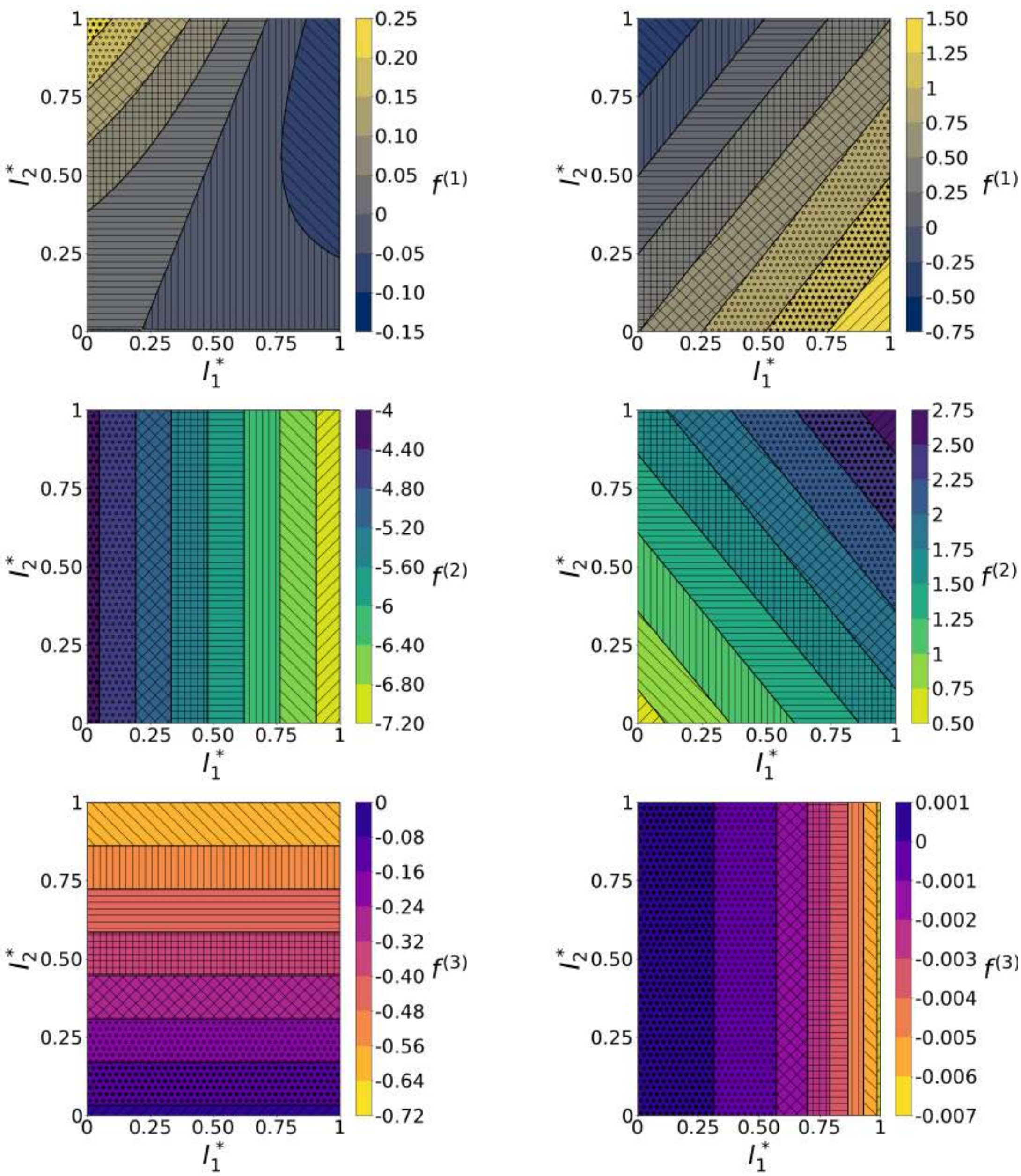

Fig. 9 Scalar $f^{(1)}$, $f^{(2)}$ and $f^{(3)}$ as function of the normalized invariants I_1^* and I_2^*. CSA+a_{ij}_20 and CSA+a_{ij}_25 outcomes on the left and right, respectively.

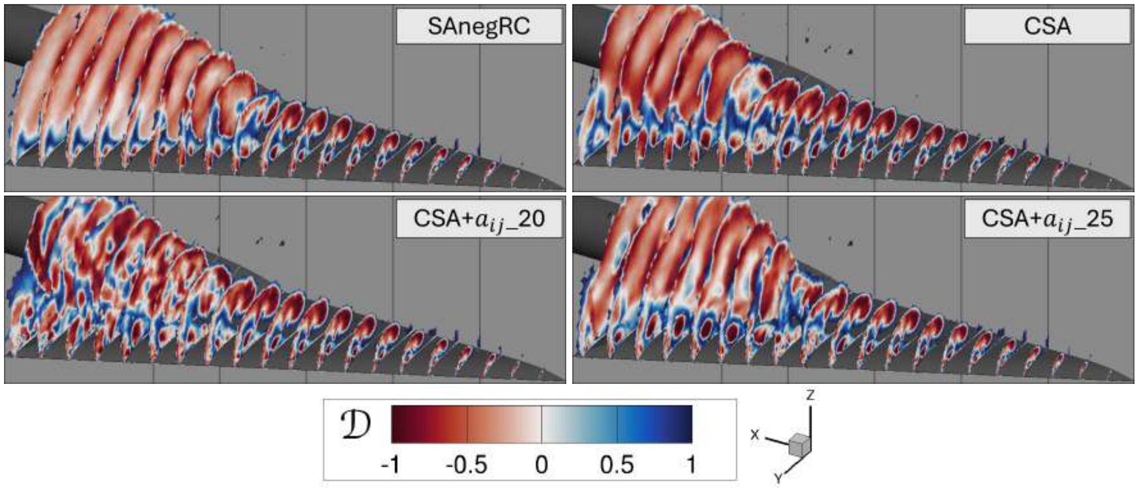

Fig. 10 VFE-2 training outcomes at α = 25.6°: normalized invariant of the deformation tensor $\mathcal{D}$. Black lines in the background are marking the probing locations, ξ, presented in Fig. 2.

In this discussion, it is essential to identify regions where either strain or vorticity dominates, to better understand the behavior of the invariants in vortex-dominated flows. To this end, the normalized second invariant $\mathcal{D}$ of the velocity gradient tensor is illustrated in Fig. 10, which provides a clear distinction between vorticity-dominated and strain rate-dominated flow regimes. The normalized invariant of the velocity gradient tensor is defined as follows:

$$\mathcal{D} = \frac{S_{ij}S_{ij} - W_{ij}W_{ij}}{S_{ij}S_{ij} + W_{ij}W_{ij}} \tag{15}$$

where $\mathcal{D} \rightarrow 1$ indicates strain-dominated flow, while $\mathcal{D} \rightarrow -1$ indicates vorticity-dominated flow. Figure 10 highlights key features of the flow based on $\mathcal{D}$. The core of the primary and secondary vortices is a vorticity-dominated region. In contrast, the shear layer detaching from the leading edge and rolling up to form the primary vortex is dominated by the strain rate. These components mix at the edges of the primary and secondary vortices, forming a region where the two contributions balance each other, resulting in a zero value of $\mathcal{D}$. Furthermore, around $\xi = 0.6$, the primary vortex breakdown is evident as a sudden shift from vorticity-dominated to strain-dominated flow, before transitioning back to vorticity dominance further downstream.

Figure 9 shows that CSA+a_{ij}_20 exhibits negative values of $f^{(1)}$ in strain-dominated regions, which correspond to high values of I_1. In contrast, CSA+a_{ij}_25 shows negative values of $f^{(1)}$ in vorticity-dominated regions, as indicated by high values of I_2. This highlights an opposite correction of the model in regions affected by opposite signs of $\mathcal{D}$, explaining why models trained at different AoA are not interchangeable and yield less accurate results when applied to cases outside their training set. The scalar $f^{(2)}$ in CSA+a_{ij}_20 solely depending on strain, remains generally negative, and decreases further with increasing strain levels. Conversely, $f^{(2)}$ in CSA+a_{ij}_25 remains positive, and it does not differentiate between strain- and vorticity-dominated regions, indicating that $f^{(2)}$ depends only on the sum of strain and vorticity magnitudes. Consequently, equal magnitudes of I_1 or I_2 will yield the same value of $f^{(2)}$. This suggests that $f^{(2)}$ scales proportionally with the magnitude of the velocity gradient. Combining the effects of $f^{(1)}$ and $f^{(2)}$, both in CSA+a_{ij}_20 and CSA+a_{ij}_25, the modification will have a more mitigated effect in vorticity-dominated regions, such as primary and secondary vortices, while significantly impacting strain-dominated regions, such as the shear layer. However, the signs of these modifications are opposite: in CSA+a_{ij}_20, turbulence in the shear layer is strongly increased, whereas in CSA+a_{ij}_25, it is reduced. While $f^{(1)}$ was the most complex scalar in CSA+a_{ij}_20, $f^{(3)}$ exhibits non-linear behavior in CSA+a_{ij}_25, but depends only on I_1. Both models demonstrate distinct dependencies on the invariants I_1 or I_2, respectively. The scalar $f^{(3)}$ approaches zero near equilibrium or at low vorticity levels and decreases further with increasing vorticity for CSA+a_{ij}_20. In contrast, CSA+a_{ij}_25 exhibits a decrease in $f^{(3)}$ with increasing strain, transitioning to negative values when $I_1 > 0.2$. The interpretable GEP expressions revealed a fundamental insight: successful turbulence corrections for delta wing flows must be inherently regime-dependent, with qualitatively different behaviors in strain- versus vorticity-dominated regions. Rather than indicating model inadequacy, this finding demonstrates that physics-based corrections naturally adapt to local flow conditions. This motivates extending the CFD-driven multi-case training to include $\mathcal{D}$ explicitly alongside I_1 and I_2, and to span multiple AoA so that regime adaptivity could be learned directly.

As highlighted in the previous analysis, the genetically optimized models exhibit distinct dependencies on the invariants I_1 and I_2, with varying weights in the respective formulations of the scalars $f^{(k)}$. However, their individual effects on the flow cannot be assessed. In combination with the basis tensors, which themselves depend on strain and/or vorticity, the effects are scaled uniquely. To illustrate this behaviour, the CSA+a_{ij}_25 model is examined. Individual simulations are conducted in which certain scalars remain unaltered while others are set to zero, testing all possible combinations. Figure 11 shows the spanwise pressure coefficient distribution on the VFE2 as a result of the investigation of scalar and tensor combinations.

The interpretable nature of GEP expressions enabled this systematic investigation of tensor combinations, directly validating the coupled CSA+a_{ij} modeling approach. This interpretability-driven validation provides confidence that the coupled model form captures the necessary physics through synergistic tensor interactions. Notably, no single combination replicates the complete combination of all scalars and the basis tensor in the CSA+a_{ij}_25; no individual tensor component can capture the complete flow physics, addressing concerns about model adequacy for this family of flows. The scalar $f^{(3)}$ alone has little effect on the flow and closely matches the baseline model. Similarly, in the combination $f^{(2)}\&f^{(3)}$, $f^{(3)}$ appears to have a negligible effect, as $f^{(2)}$ alone produces a similar outcome. However, when considering $f^{(1)}\&f^{(3)}$, the presence of $f^{(3)}$ is no longer negligible, as $f^{(1)}$ alone does not follow the same trend. Upstream of $\xi = 0.6$, $f^{(1)}$ and $f^{(2)}$ exhibit similar behavior, as also indicated by the combination $f^{(1)}\&f^{(2)}$. However, downstream of $\xi = 0.6$, their behavior diverges, which may be linked to the onset of primary vortex breakdown.

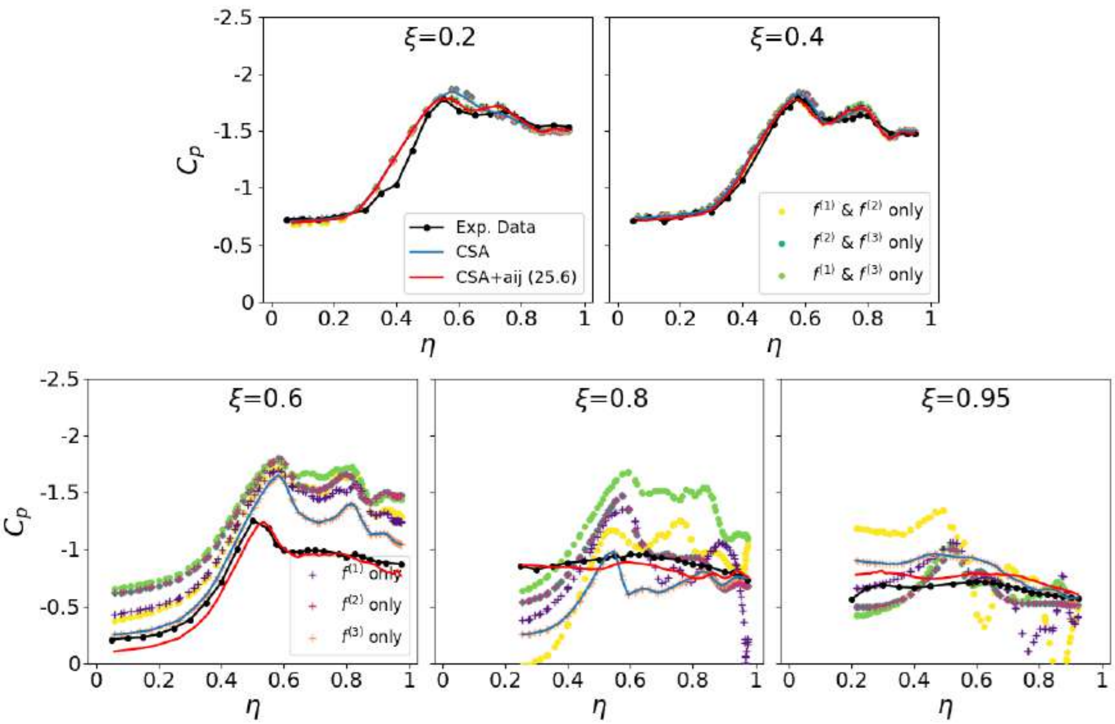

Fig. 11 Investigations of scalar and tensor combinations: spanwise pressure coefficient distribution at α = 25.6°.

The eddy viscosity is examined to assess the impact of the optimization on the turbulence prediction. The contours of $R_t = \mu_t/\mu$ are plotted, where μ is the molecular dynamic viscosity. Figures 12 and 13 shows the outcomes at α = 20.5° and 25.6°, respectively. In RANS computations, regions with large eddy viscosity values typically correspond to areas of intense vortex motion, where substantial turbulence energy is produced as a result of strong flow rotation and deformation. This behavior reflects the inherent tendency of RANS models to associate elevated eddy viscosity with regions of high vorticity and strain. Consequently, such a correlation can influence the accuracy of turbulence predictions, particularly in highly rotational flows [64].

Across all turbulence models, elevated eddy viscosity levels initially appear in the shear layer before developing in the primary vortex region. For CSA+a_{ij}_25, turbulence production remains negligible in regions containing coherent structures, as indicated by consistently low eddy viscosity values. In contrast, SAnegRC and CSA exhibit different distributions of eddy viscosity within the primary vortex. CSA predicts elevated eddy viscosity values outboard and within the shear layer, whereas the SAnegRC outcomes indicate that this region extends further inboard, closer to the primary vortex. For CSA+a_{ij}_25, the highest eddy viscosity values are initially observed in the regions of the primary vortex following its breakdown. Therefore, this model counteracts the unphysical generation of eddy viscosity in regions of the intact coherent vortex motion and instead correctly predicts turbulence only after vortex breakdown. This behavior differs from other turbulence models, where elevated eddy viscosity levels first appear in the shear layer. The $f^{(1)}$ and $f^{(2)}$ behaviors are reflected in the observed eddy viscosity values: in CSA+a_{ij}_20, the eddy viscosity in the shear layer is notably increased, leading to enhanced turbulence generation, whereas in CSA+a_{ij}_25, the eddy viscosity is reduced in the same region, resulting in a weaker turbulence response. These opposite trends highlight the distinct corrections applied in each case, evidencing regime-dependent corrections. This interpretable understanding directly informed our analysis methodology and validates the necessity of the coupled approach, where both the Reynolds stress tensor and the turbulence production term are simultaneously modified to capture the complex strain-vorticity interactions characteristic of vortical flows.

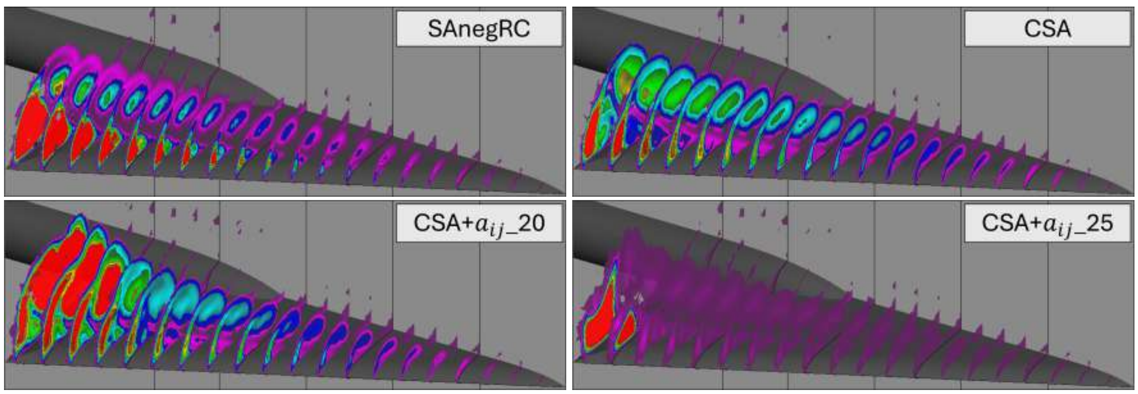

Fig. 12 VFE-2 training outcomes at α = 20.5°: eddy viscosity ratio, R_t.

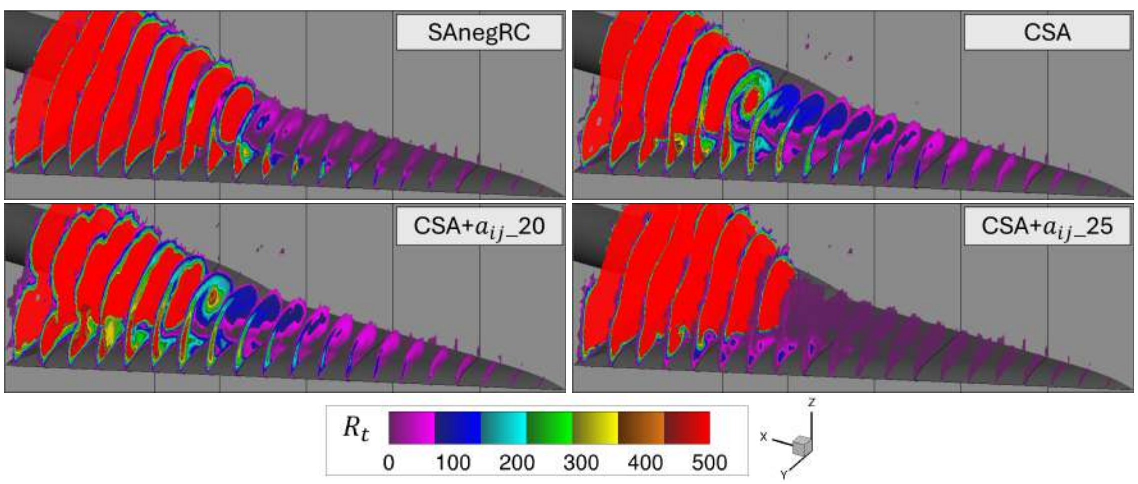

Fig. 13 VFE-2 training outcomes at α = 25.6°: eddy viscosity ratio, R_t.

B. Validation with double and triple-delta wing configurations

For validation, the DW1 and DW2 configurations are considered to assess the predictive accuracy of the turbulence models. The complex flow physics associated with the DW1 and DW2 configurations poses a significant challenge for turbulence models, and its detailed description is available in [14, 22, 54]. These validation results represent a particularly challenging test of model generalizability. The CSA+a_{ij} models, trained exclusively under symmetric flow conditions, are required to predict aerodynamic behavior under asymmetric conditions that generate non-zero roll moments and complex three-dimensional flow interactions. This extrapolation test assesses whether the physics captured during symmetric training can be successfully extended to fundamentally different flow topologies involving cross-flow effects and asymmetric vortex interactions.

The aerodynamic coefficient predictions are based on RANS calculations, and the results are presented in Fig. 14 with Fig. 15 showing the relative deviation (%) between numerical and experimental aerodynamic coefficients for DW1 and DW2 delta wing configurations. The lift coefficient, C_L, is shown on the left, the rolling moment coefficient, C_{m_x}, in the middle, and the pitching moment coefficient, C_{m_y}, on the right. Accurately predicting the aerodynamic coefficients depends on the model's ability to represent specific flow phenomena accurately. Angles of attack of 12°, 16°, 20°, 24°, and 28° are of particular interest, as these capture all the relevant flow regimes and require accurate predictions of several critical flow phenomena such as shear-layer separation, leading-edge vortex formation, vortex breakdown, and vortex-vortex interactions.

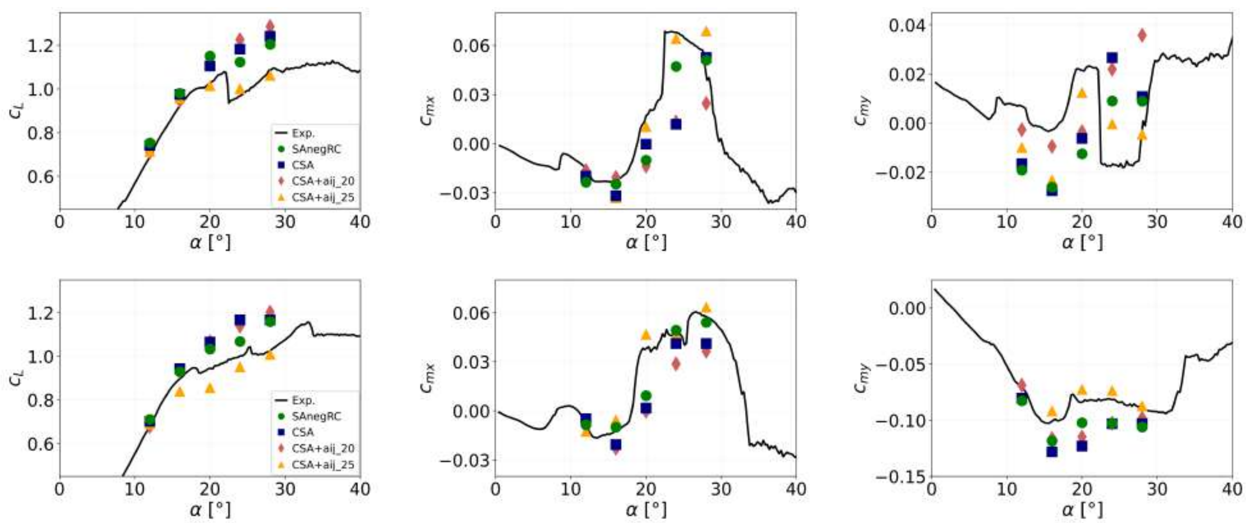

Fig. 14 Aerodynamic coefficients prediction of the DW1 triple-delta wing (on the top) and DW2 double-delta wing (on the bottom) configuration under asymmetric and transonic flow conditions with $Ma = 0.85$, Re $= 12.53 \times 10^6$ and $\beta = 5°$.

Examining C_L for the DW1 configuration first, all models, except for CSA+a_{ij}_25, fail to accurately predict the trend of the lift coefficient. While the models provide reasonably accurate results at the lower AoA of 12° and 16°, they tend to overpredict the lift coefficient at higher AoA and fail to capture the lift reduction following the breakdown of the primary vortex on the windward wing [14]. Regarding the prediction of the moment coefficients, no single model performs best across all AoAs. However, two key considerations must be taken into account. The CSA+a_{ij}_25 model seems to provide the closest match to the experimental data for C_{m_x} and additionally captures the qualitative drop in C_{m_y} for $\alpha > 20°$. Moreover, the CSA+a_{ij}_20 model yields the most accurate results for $\alpha = 12°$ and 16°. For the DW2 configuration, CSA+a_{ij}_25 exhibits the best overall performance. Even at a low angle of attack like $\alpha = 12°$, well outside the training case, CSA+a_{ij}_25 performs with comparable accuracy as the CSA baseline model or better. In contrast, CSA+a_{ij}_20 generally underperforms compared to the CSA baseline model, except for $\alpha = 12°$ and $16°$, where it improves the accuracy of the RANS outcomes and provides the closest match to the experimental data.

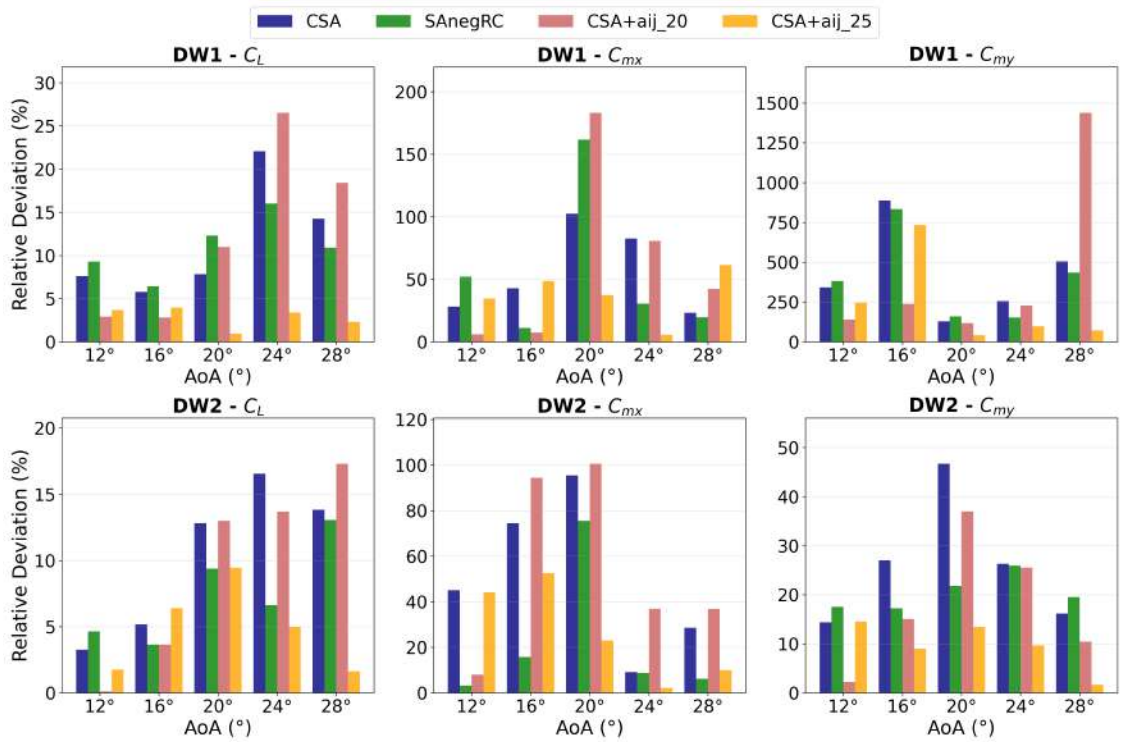

Fig. 15 Grouped bar charts of relative deviation (%) between numerical and experimental aerodynamic coefficients for DW1 and DW2 delta wing configurations. Each row corresponds to a configuration; columns show lift coefficient (C_L), rolling-moment coefficient (C_{m_x}), and pitching-moment coefficient (C_{m_y}) deviations at 5 angles of attack ($12°, 16°, 20°, 24°$, **and** $28°$)**. Bars are grouped by turbulence-model method (CSA, SAnegRC, CSA+a_{ij}_20, CSA+a_{ij}_25), with y-axes individually scaled to each coefficient's error range.**

These results highlight the challenge of developing a model that performs well under all conditions within a combat aircraft's flight envelope due to the complexity of the underlying physical phenomena. By analyzing the results of both configurations, it is evident that CSA+a_{ij}_20 achieves the best performance at $\alpha = 12°$ and $16°$, whereas CSA+a_{ij}_25 provides higher accuracy at higher AoAs (20°, 24°, and 28°). This behavior can be attributed to the physical phenomena considered during training and those targeted in the validation cases. As previously discussed, ensuring consistency between the physical phenomena present during training and those in the validation phase is essential. Specifically, CSA+a_{ij}_20, trained without accounting for vortex breakdown on VFE-2, enhances baseline predictions at lower angles of attack, where DW1 and DW2 do not exhibit vortex breakdown over the wings [14, 54]. In contrast, CSA+a_{ij}_25 outperforms at higher angles when vortex breakdown is present. Nevertheless, the approach proposed in this study, particularly the CSA+a_{ij}_25 model, demonstrates a certain level of generalizability and provides a solid foundation for future optimizations and investigations.

The flow physics are depicted in Figs. 16 and 17. Taking the above considerations into account, the CSA+a_{ij}_20 results are shown at $\alpha = 16°$, while the CSA+a_{ij}_25 outcomes are presented for higher angles of attack. The instantaneous Q-criterion is employed to visualize the vortex system over the multi-wing configurations under various flow conditions, enabling the identification of different flow regimes as the angle of attack varies. The trained models outperform the standard RANS outcomes reported in the literature [14, 22, 54], providing a more accurate representation of the flow phenomena occurring over the wing at transonic conditions. These results lay the solid foundation for further analysis and model development, particularly in the context of optimization strategies.

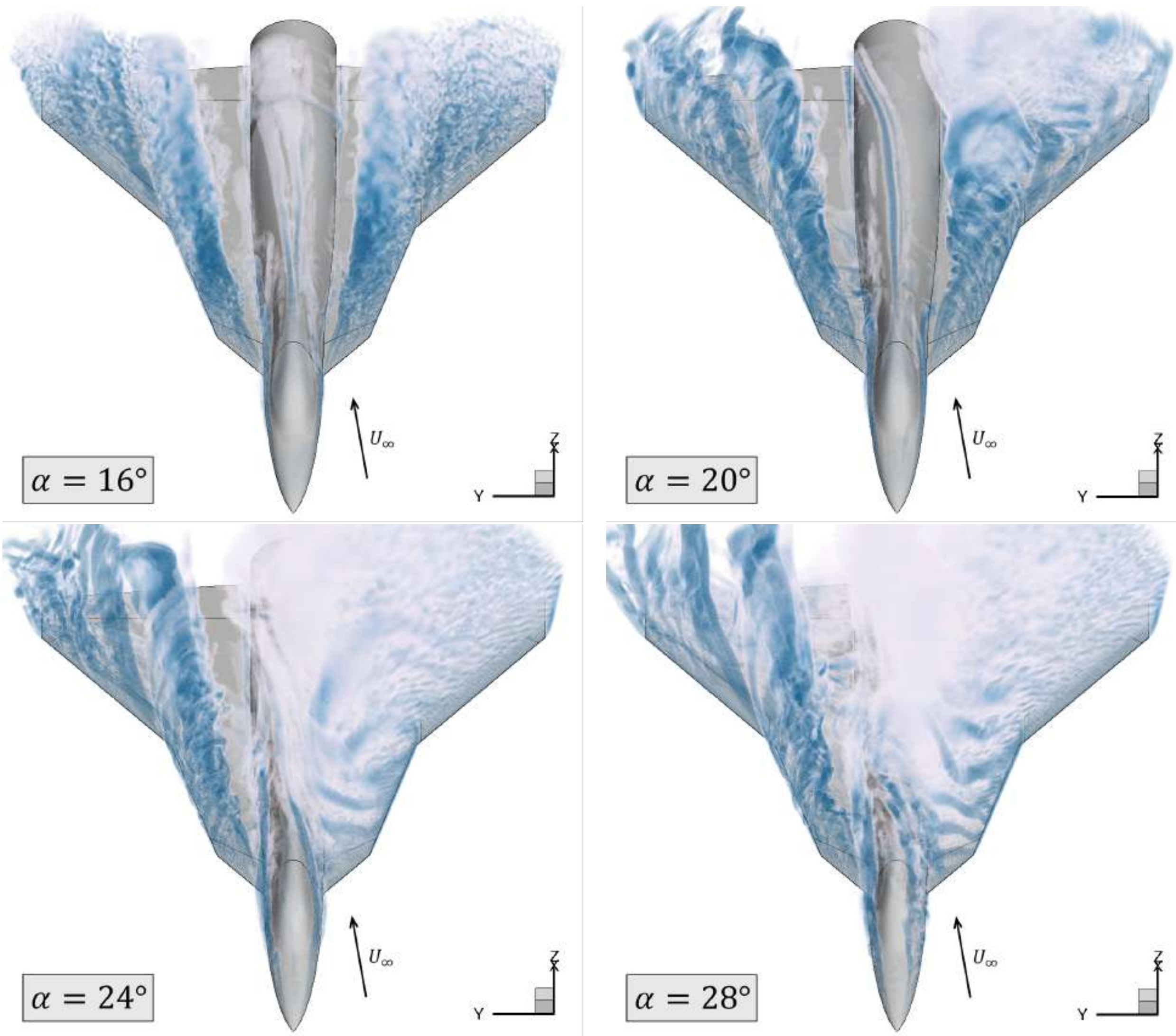

Fig. 16 Instantaneous Q-criterion iso-surfaces at different angles of attack on the DW1 configuration. CSA+a_{ij}_20 at $\alpha = 16°$; CSA+a_{ij}_25 for higher angles of attack.

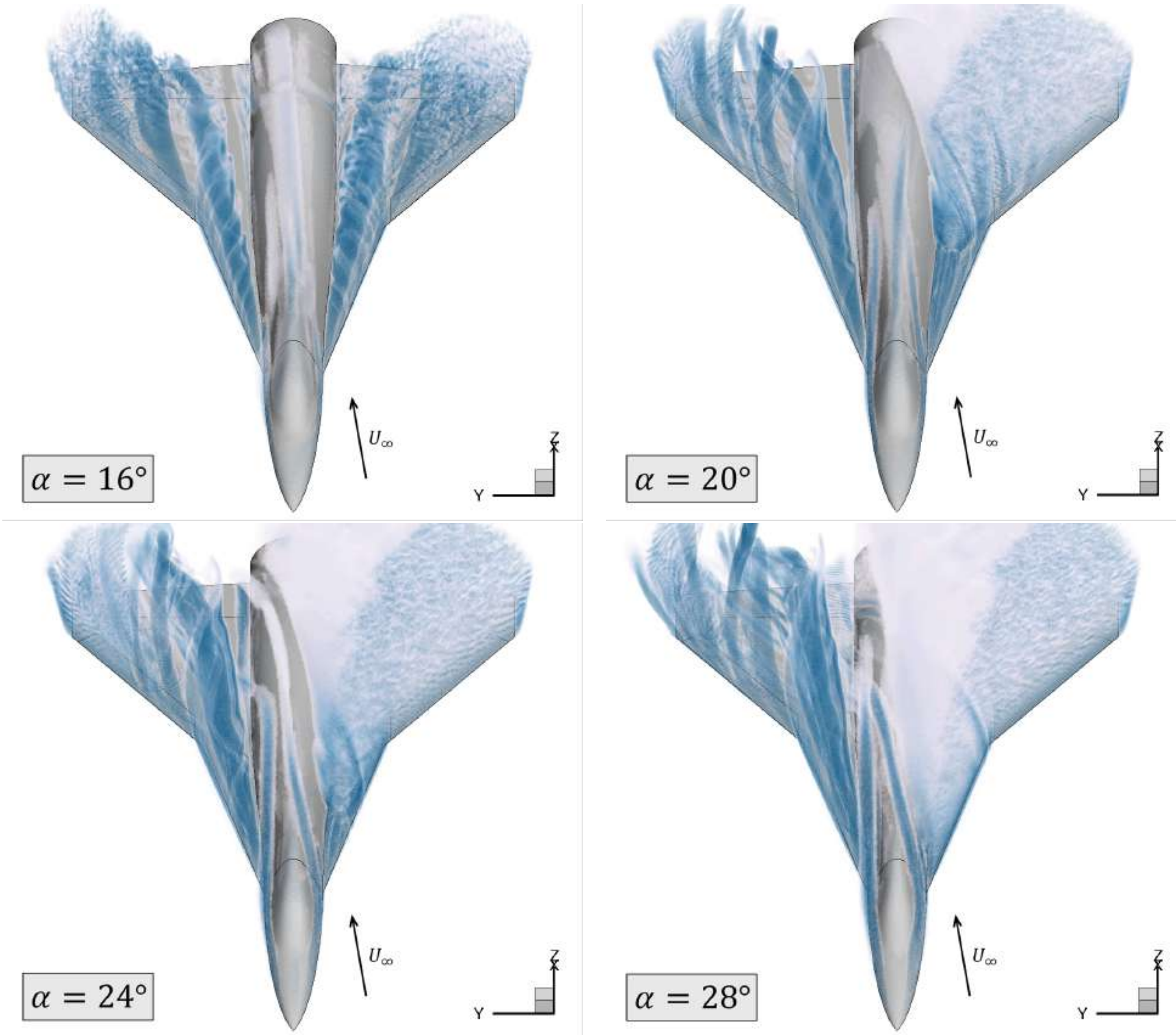

Fig. 17 Instantaneous Q-criterion iso-surfaces at different angles of attack on the DW2 configuration. CSA+a_{ij}_20 at $\alpha = 16°$; CSA+a_{ij}_25 for higher angles of attack.

V. Conclusion and Outlook

The VFE-2 delta wing configuration has been numerically investigated using RANS calculations under symmetric flow conditions to optimize turbulence modeling. A CFD-driven GEP approach is employed to enhance a one-equation turbulence model through two key strategies: (i) extending the Boussinesq hypothesis to represent Reynolds stress anisotropy better, and (ii) improving the modeling of turbulence production and dissipation. This is achieved using the CSA model [49], in which the production term incorporates a nonlinear extension of the Boussinesq approximation. GEP is used to discover an improved anisotropic stress tensor a^*_{ij}, which simultaneously optimizes both the Reynolds stress representation and the turbulence production term in the $\tilde{\nu}$ transport equation. The resulting CSA+a_{ij} model has been trained at two angles of attack ($\alpha = 20.5°$ and $\alpha = 25.6°$) and validated against experimental data. The simulations have been conducted at $Ma = 0.80$ and $\mathrm{Re} = 2 \times 10^6$. The turbulence models have then been validated by applying them to the DW1 (triple-delta wing) and DW2 (double-delta wing) configurations under transonic and asymmetric flow conditions ($Ma = 0.85$, $\mathrm{Re} = 12.53 \times 10^6$) for multiple angles of attack ($\alpha = 12°$, $16°$, $20°$, $24°$, and $28°$). To the best of our knowledge, this work represents the first application of a CFD-driven turbulence modeling approach to a complex three-dimensional external aerodynamic configuration at transonic speeds and high Reynolds numbers. The results demonstrate the potential of data-driven modeling in improving predictive capabilities in challenging aerodynamic regimes.

Beyond enabling automated discovery, GEP interpretability served as both a diagnostic tool and an active driver of model validation. The explicit expressions enabled systematic decomposition of model contributions, revealing the physics-based rationale for regime-dependent corrections. This interpretability-driven analysis validated that the CSA+aij model captures essential flow physics through coordinated tensor interactions, demonstrating that apparent model "incompatibility" between training cases actually reflects the physics requirement for adaptive corrections in different flow regimes. The interpretable nature of GEP expressions proved instrumental for model validation and physical understanding. The symbolic expressions revealed that: (i) no single tensor modification can replicate the complete model performance; (ii) regime-dependent behavior is a physics requirement; (3) the opposite corrections in strain- vs vorticity-dominated regions reflect proper adaptation to local flow physics. These interpretability-driven insights provided both confidence in the coupled model design and a framework for future improvements, demonstrating how transparent machine learning can advance turbulence modeling through physics-based validation rather than black-box optimization. Future work will implement a multi-case, multi-AoA CFD-driven training that explicitly includes $\mathcal{D}$ together with I_1 and I_2 to learn regime adaptivity and strengthen generalization across operating conditions, following Fang et al. [48], who included several flow features within multi-case training to improve model transfer across test cases.

The findings underscore the challenge of developing a model that maintains high performance across all conditions within a combat aircraft's flight envelope, due to the complexity of the governing physical phenomena. The analysis reveals that CSA+a_{ij}_20 performs best at lower angles of attack, at $\alpha = 12°$ and $16°$, while CSA+a_{ij}_25 achieves higher accuracy at larger angles ($20°$, $24°$, and $28°$). This variation arises from the physical phenomena considered during model training and validation. The results indicate that the applicability of the trained models is primarily governed by the underlying physical phenomena rather than the specific geometries considered. Generalizability across different geometries and test cases is achieved when the relevant physical phenomena are accurately captured during training. However, discrepancies may arise when flight conditions change, as the training process may model physical phenomena that are not present in the validation cases. These findings emphasize the importance of selecting appropriate training conditions to ensure robust and reliable turbulence modeling for industrial applications.

Including primary vortex breakdown phenomena in the training process is crucial for extending the model's applicability beyond the training dataset. The CSA+a_{ij}_25 model, trained to account for vortex breakdown, successfully predicts this phenomenon in various configurations, including highly intricate cases. However, this capability comes at the cost of the model predicting reduced aerodynamic efficiency under different flight conditions. This highlights the need for multi-case training incorporating additional AoA and dominant flow physics to achieve balanced performance. These findings underscore the importance of multi-case training strategies and flow-physics-aware model design to achieve a balanced and robust performance. The validation under asymmetric flow conditions demonstrates the models' ability to extrapolate beyond their symmetric training conditions. The successful improvement of roll and pitching moment prediction with asymmetric flow, despite the absence of such conditions during training, indicates that the GEP-learned corrections capture fundamental physics that extend to more complex three-dimensional flow configurations.

The CSA+a_{ij} model has exhibited substantial improvements over the baseline model due to its coupled nature. However, inconsistencies in accuracy and occasional large deviations from experimental data have been observed. This could suggest the need for improved flow feature selection. A potential solution to this issue could involve incorporating all ten basis tensors and the five invariants of the velocity tensor, as suggested for three-dimensional cases based on Pope's theory [55]. However, this approach would significantly increase the computational cost of training, necessitating a trade-off between accuracy and efficiency. Besides, considering an alternative or an additional optimization target in the training process may be beneficial. The baseline CSA model's formulation also suggests that inaccuracies may stem from the calibration of constants used in both turbulence models, and further studies will be conducted on this research topic. While the current study focuses on industrially relevant delta wing applications, we acknowledge that comprehensive validation on canonical vortical flow and free shear layer cases would strengthen model interpretability. Our earlier work demonstrated the efficacy of the GEP framework on canonical wall-bounded flows [49]. Ongoing work incorporates canonical vortical test cases into multi-case training strategies to enhance model generalizability across fundamental flow configurations.

Despite these challenges, the present work demonstrates the significant potential of combining machine learning with turbulence modeling. GEP-enabled CFD-driven frameworks offer not only improved predictive accuracy but also a pathway toward interpretable, generalizable, and physically informed models. This approach establishes a promising foundation for the broader adoption of genetic algorithms and symbolic regression in turbulence closure development, particularly in the context of real-world, high-Reynolds-number aerodynamic applications. It represents a pioneering effort in applying machine learning-based turbulence modeling to highly complex industrial challenges, highlighting its potential for advancing predictive capabilities in engineering applications.

Acknowledgment

We gratefully acknowledge the financial support from Deutscher Akademischer Austauschdienst (DAAD) for this research (grant number 57694189). Our gratitude extends to the German Aerospace Center for supplying the DLR TAU-Code, which was instrumental in the numerical analysis of this study. The contribution of Ennova Technologies Inc. in providing meshing software is also earnestly acknowledged. We thank the Gauss Centre for Supercomputing for their generous allocation of computing time on the GCS Supercomputer SuperMUC at the Leibniz Supercomputing Centre under the account number pn29xa. Lastly, the visit to the University of Melbourne of the first author was supported by the German Federal Ministry of Defence.

References

[1] Hitzel, S. M., Winkler, A., and Hövelmann, A., "Vortex flow aerodynamic challenges in the design space for future fighter aircraft," *New Results in Numerical and Experimental Fluid Mechanics XII: Contributions to the 21st STAB/DGLR Symposium, Darmstadt, Germany, 2018*, Springer, 2020, pp. 297–306. https://doi.org/10.1007/978-3-030-25253-3_29.

[2] Cummings, R., Schütte, A., Schmidt, S., Hummel, D., Milanov, E., Konrath, R., Zlatev, Z., Loeser, T., Simonsen, C., Oehlke, M., Anne, G., Otter, D., ROY, J.-F., Hitzel, S., Rohlf, D., Pallek, D., Roosenboom, E., Schröder, A., Petterson, K., and Perkins, S., "Assessment of Stability and Control Prediction Methods for NATO Air and Sea Vehicles," Tech. rep., 04 2012.

[3] Escudier, M., "Vortex breakdown: Observations and explanations," *Progress in Aerospace Sciences*, Vol. 25, No. 2, 1988, p. 189–229. https://doi.org/10.1016/0376-0421(88)90007-3.

[4] Schütte, A., Hummel, D., and Hitzel, S. M., "Flow physics analyses of a generic unmanned combat aerial vehicle configuration," *Journal of Aircraft*, Vol. 49, No. 6, 2012, pp. 1638–1651. https://doi.org/10.2514/1.C031386.

[5] Schiavetta, L. A., Boelens, O. J., Crippa, S., Cummings, R. M., Fritz, W., and Badcock, K. J., "Shock effects on delta wing vortex breakdown," *Journal of aircraft*, Vol. 46, No. 3, 2009, pp. 903–914. https://doi.org/10.2514/1.38792.

[6] Schütte, A., Boelens, O. J., Oehlke, M., Jirásek, A., and Loeser, T., "Prediction of the flow around the X-31 aircraft using three different CFD methods," *Aerospace Science and Technology*, Vol. 20, No. 1, 2012, pp. 21–37. https://doi.org/10.1016/j.ast.2011.07.014.

[7] Cummings, R. M., Forsythe, J. R., Morton, S. A., and Squires, K. D., "Computational challenges in high angle of attack flow prediction," *Progress in Aerospace Sciences*, Vol. 39, No. 5, 2003, pp. 369–384. https://doi.org/10.1016/S0376-0421(03)00041-1.

[8] Cummings, R. M., and Schütte, A., "Detached-Eddy Simulation of the vortical flow field about the VFE-2 delta wing," *Aerospace Science and Technology*, Vol. 24, No. 1, 2013, pp. 66–76. https://doi.org/10.1016/j.ast.2012.02.007.

[9] Hummel, D., "Review of the second international vortex flow experiment (VFE-2)," *46th AIAA Aerospace Sciences Meeting and Exhibit*, 2008, p. 377. https://doi.org/10.2514/6.2008-377.

[10] Fritz, W., and Cummings, R., "What was learned from the numerical simulations for the VFE-2," *46th AIAA Aerospace Sciences Meeting and Exhibit*, 2008, p. 399. https://doi.org/10.2514/6.2008-399.

[11] Werner, M., Schütte, A., and Weiss, S., "Turbulence Model Effects on the Prediction of Transonic Vortex Interaction on a Multi-Swept Delta Wing," AIAA SCITECH Forum, San Diego, CA, 2022. https://doi.org/10.2514/6.2022-0295.

[12] Werner, M., Rein, M., Richter, K., and Weiss, S., "Experimental and numerical analysis of the aerodynamics and vortex interactions on multi-swept delta wings," *CEAS Aeronautical Journal*, 2023, pp. 1–12. https://doi.org/10.1007/s13272-023-00678-7.

[13] Moioli, M., Breitsamter, C., and Sørensen, K. A., "Parametric data-based turbulence modelling for vortex dominated flows," *International Journal of Computational Fluid Dynamics*, Vol. 33, No. 4, 2019, pp. 149–170. https://doi.org/10.1080/10618562.2019.1617857.

[14] Di Fabbio, T., Tangermann, E., and Klein, M., "Investigation of transonic aerodynamics on a triple-delta wing in side slip conditions," *CEAS Aeronautical Journal*, 2022. https://doi.org/10.1007/s13272-022-00571-9.

[15] Di Fabbio, T., Tangermann, E., and Klein, M., "Analysis of the vortex-dominated flow field over a delta wing at transonic speed," *The Aeronautical Journal*, 2023, p. 1–18. https://doi.org/10.1017/aer.2023.30.

[16] Moioli, M., Breitsamter, C., and Sørensen, K., "Turbulence Modeling for Leading-Edge Vortices: an Enhancement based on Experimental Data," AIAA SciTech Forum, Orlando, FL, 2020. https://doi.org/10.2514/6.2020-1032.

[17] Boussinesq, J. V., *Essai sur la théorie des eaux courantes*, Impr. nationale, 1877.

[18] Schmitt, F. G., "About Boussinesq's turbulent viscosity hypothesis: historical remarks and a direct evaluation of its validity," *Comptes Rendus Mécanique*, Vol. 335, No. 9-10, 2007, pp. 617–627. https://doi.org/10.1016/j.crme.2007.08.004, URL https://hal.science/hal-00264386.

[19] Wilcox, D. C., et al., *Turbulence modeling for CFD*, Vol. 2, DCW industries La Canada, CA, 1998.

[20] Spalart, P., and Allmaras, S., "A one-equation turbulence model for aerodynamic flows," *30th aerospace sciences meeting and exhibit*, 1992, p. 439. https://doi.org/10.2514/6.1992-439.

[21] Menter, F. R., "Two-equation eddy-viscosity turbulence models for engineering applications," *AIAA Journal*, Vol. 32, No. 8, 1994, p. 1598–1605. https://doi.org/10.2514/3.12149.

[22] Di Fabbio, T., Rajkumar, K., Tangermann, E., and Klein, M., "Towards the understanding of vortex breakdown for improved RANS turbulence modeling," *Aerospace Science and Technology*, 2024. https://doi.org/10.1016/j.ast.2024.108973.

[23] Rumsey, C., and Coleman, G., "NASA Symposium on Turbulence Modeling: Roadblocks, and the Potential for Machine Learning," Tech. rep., 2022. URL https://turbmodels.larc.nasa.gov/Turb-prs2022/NASA-TM-20220015595final.pdf.

[24] Spalart, P. R., “Strategies for turbulence modelling and simulations,” *International Journal of Heat and Fluid Flow*, Vol. 21, No. 3, 2000, pp. 252–263. https://doi.org/10.1016/S0142-727X(00)00007-2.

[25] Parmar, B., Peters, E., Jansen, K. E., Doostan, A., and Evans, J. A., “Generalized non-linear eddy viscosity models for data-assisted Reynolds stress closure,” *AIAA Scitech 2020 Forum*, 2020, p. 0351. https://doi.org/10.2514/6.2020-0351.

[26] Alauzet, F., and Spalart, P., “A new rotation correction for the Spalart-Allmaras model to improve off-body vortex prediction and vortex-vortex interaction effects,” *AIAA SCITECH 2024 Forum*, 2024, p. 1335. https://doi.org/10.2514/6.2024-1335.

[27] Pope, S. B., “A more general effective-viscosity hypothesis,” *Journal of Fluid Mechanics*, Vol. 72, No. 2, 1975, p. 331–340. https://doi.org/10.1017/S0022112075003382.

[28] Rumsey, C. L., Carlson, J.-R., Pulliam, T. H., and Spalart, P. R., “Improvements to the Quadratic Constitutive Relation Based on NASA Juncture Flow Data,” *AIAAJ*, Vol. 58, 2020. https://doi.org/10.2514/1.J059683.

[29] Duraisamy, K., Iaccarino, G., and Xiao, H., “Annual Review of Fluid Mechanics Turbulence Modeling in the Age of Data,” *Annu. Rev. Fluid Mech*, Vol. 51, 2019, pp. 357–377. https://doi.org/10.1146/annurev-fluid-010518-040547, URL https://www.annualreviews.org/content/journals/10.1146/annurev-fluid-010518-040547.

[30] Edeling, W. N., Cinnella, P., Dwight, R. P., and Bijl, H., “Bayesian estimates of parameter variability in the k-ϵ turbulence model,” *Journal of Computational Physics*, Vol. 258, 2014, pp. 73–94. https://doi.org/10.1016/j.jcp.2013.10.027.

[31] Zhang, Z. J., and Duraisamy, K., “Machine learning methods for data-driven turbulence modeling,” *22nd AIAA computational fluid dynamics conference*, 2015, p. 2460. https://doi.org/10.2514/6.2015-2460.

[32] Wang, J.-X., Wu, J.-L., and Xiao, H., “Physics-informed machine learning approach for reconstructing Reynolds stress modeling discrepancies based on DNS data,” *Physical Review Fluids*, Vol. 2, No. 3, 2017. https://doi.org/10.1103/PhysRevFluids.2.034603.

[33] Ling, J., Kurzawski, A., and Templeton, J., “Reynolds averaged turbulence modelling using deep neural networks with embedded invariance,” *Journal of Fluid Mechanics*, Vol. 807, 2016, pp. 155–166. https://doi.org/10.1017/jfm.2016.615.

[34] Zhang, Z., Ye, S., Yin, B., Song, X., Wang, Y., Huang, C., and Chen, Y., “A semi-implicit discrepancy model of Reynolds stress in a higher-order tensor basis framework for Reynolds-averaged Navier–Stokes simulations,” *AIP Advances*, Vol. 11, No. 4, 2021. https://doi.org/10.1063/5.0033109.

[35] Ling, J., Jones, R., and Templeton, J., “Machine learning strategies for systems with invariance properties,” *Journal of Computational Physics*, Vol. 318, 2016, pp. 22–35. https://doi.org/10.1016/j.jcp.2016.05.003.

[36] Zhang, Z., Song, X.-d., Ye, S.-r., Wang, Y.-w., Huang, C.-g., An, Y.-r., and Chen, Y.-s., “Application of deep learning method to Reynolds stress models of channel flow based on reduced-order modeling of DNS data,” *Journal of Hydrodynamics*, Vol. 31, 2019, pp. 58–65. https://doi.org/10.1007/s42241-018-0156-9.

[37] Singh, A. P., Duraisamy, K., and Zhang, Z. J., “Augmentation of turbulence models using field inversion and machine learning,” *55th AIAA Aerospace Sciences Meeting*, 2017, p. 0993. https://doi.org/10.2514/6.2017-0993.

[38] Schmelzer, M., Dwight, R. P., and Cinnella, P., "Discovery of algebraic Reynolds-stress models using sparse symbolic regression," *Flow, Turbulence and Combustion*, Vol. 104, 2020, pp. 579–603. https://doi.org/10.1007/s10494-019-00089-x.

[39] Akolekar, H. D., Weatheritt, J., Hutchins, N., Sandberg, R. D., Laskowski, G., and Michelassi, V., "Development and use of machine-learnt algebraic Reynolds stress models for enhanced prediction of wake mixing in low-pressure turbines," *Journal of Turbomachinery*, Vol. 141, No. 4, 2019. https://doi.org/10.1115/1.4041753.

[40] Thompson, R. L., Sampaio, L. E. B., de Bragança Alves, F. A., Thais, L., and Mompean, G., "A methodology to evaluate statistical errors in DNS data of plane channel flows," *Computers & Fluids*, Vol. 130, 2016, pp. 1–7. https://doi.org/10.1016/j.compfluid.2016.01.014.

[41] Poroseva, S. V., Colmenares F, J. D., and Murman, S. M., "On the accuracy of RANS simulations with DNS data," *Physics of Fluids*, Vol. 28, No. 11, 2016. https://doi.org/10.1063/1.4966639.

[42] Singh, A. P., and Duraisamy, K., "Using field inversion to quantify functional errors in turbulence closures," *Physics of Fluids*, Vol. 28, No. 4, 2016. https://doi.org/10.1063/1.4947045.

[43] Parish, E. J., and Duraisamy, K., "A paradigm for data-driven predictive modeling using field inversion and machine learning," *Journal of computational physics*, Vol. 305, 2016, pp. 758–774. https://doi.org/10.1016/j.jcp.2015.11.037.

[44] Wu, J.-L., Xiao, H., and Paterson, E., "Physics-informed machine learning approach for augmenting turbulence models: A comprehensive framework," *Physical Review Fluids*, Vol. 3, No. 7, 2018, p. 074602. https://doi.org/10.1103/PhysRevFluids.3.074602.

[45] Tracey, B. D., Duraisamy, K., and Alonso, J. J., "A machine learning strategy to assist turbulence model development," *53rd AIAA aerospace sciences meeting*, 2015, p. 1287. https://doi.org/10.2514/6.2015-1287.

[46] Zhu, L., Zhang, W., Kou, J., and Liu, Y., "Machine learning methods for turbulence modeling in subsonic flows around airfoils," *Physics of Fluids*, Vol. 31, No. 1, 2019. https://doi.org/10.1063/1.5061693.

[47] Zhao, Y., Akolekar, H. D., Weatheritt, J., Michelassi, V., and Sandberg, R. D., "RANS turbulence model development using CFD-driven machine learning," *Journal of Computational Physics*, Vol. 411, 2020, p. 109413. https://doi.org/10.1016/j.jcp.2020.109413.

[48] Fang, Y., Zhao, Y., Waschkowski, F., Ooi, A. S., and Sandberg, R. D., "Toward More General Turbulence Models via Multicase Computational-Fluid-Dynamics-Driven Training," *AIAA Journal*, Vol. 61, 2023, pp. 2100–2115. https://doi.org/10.2514/1.J062572.

[49] Di Fabbio, T., Fang, Y., Tangermann, E., Sandberg, R. D., and Klein, M., "Strategies for Enhancing One-Equation Turbulence Model Predictions Using Gene-Expression Programming," *Fluids*, Vol. 9, No. 8, 2024. https://doi.org/10.3390/fluids9080191.

[50] Weatheritt, J., and Sandberg, R., "A novel evolutionary algorithm applied to algebraic modifications of the RANS stress–strain relationship," *Journal of Computational Physics*, Vol. 325, 2016, pp. 22–37. https://doi.org/10.1016/j.jcp.2016.08.015.

[51] Konrath, R., Klein, C., and Schröder, A., "PSP and PIV Investigations on the VFE-2 Configuration in Sub- and Transonic Flow," 46th AIAA Aerospace Sciences Meeting and Exhibit, Reno, Nevada, 2008. https://doi.org/10.2514/6.2008-379.

[52] Hummel, D., Lamar, J., et al., "Understanding and modeling vortical flows to improve the technology readiness level for military aircraft," *NATO Research and Technology Organization/Applied Vehicle Technology, AVT-113 Task Group Final Rept. RTO-TR-AVT-113 AC/323 (AVT-113) TP/246*, 2009.

[53] Hövelmann, A., Winkler, A., Hitzel, S. M., Richter, K., and Werner, M., "Analysis of Vortex Flow Phenomena on Generic Delta Wing Planforms at Transonic Speeds," *New Results in Numerical and Experimental Fluid Mechanics XII*, Springer International Publishing, 2020, pp. 307–316. https://doi.org/10.1007/978-3-030-25253-3_30.

[54] Rajkumar, K., Di Fabbio, T., Tangermann, E., and Klein, M., "Physical aspects of vortex-shock dynamics in delta wing configurations," *Physics of Fluids*, Vol. 36, No. 6, 2024. https://doi.org/10.1063/5.0213122.

[55] Pope, S. B., "A more general effective-viscosity hypothesis," *Journal of Fluid Mechanics*, Vol. 72, No. 2, 1975, pp. 331–340. https://doi.org/10.1017/S0022112075003382.

[56] Spalart, P. R., Deck, S., Shur, M. L., Squires, K. D., Strelets, M. K., and Travin, A., "A new version of detached-eddy simulation, resistant to ambiguous grid densities," *Theoretical and computational fluid dynamics*, Vol. 20, 2006, pp. 181–195. https://doi.org/10.1007/s00162-006-0015-0.

[57] Langer, S., Schwöppe, A., and Kroll, N., "The DLR Flow Solver TAU - Status and Recent Algorithmic Developments," 52nd Aerospace Sciences Meeting, National Harbor, Maryland, USA, 2014. https://doi.org/https://doi.org/10.2514/6.2014-0080.

[58] Xu, X., Waschkowski, F., Ooi, A. S., and Sandberg, R. D., "Towards robust and accurate Reynolds-averaged closures for natural convection via multi-objective CFD-driven machine learning," *International Journal of Heat and Mass Transfer*, Vol. 187, 2022, p. 122557. https://doi.org/10.1016/j.ijheatmasstransfer.2022.122557.

[59] Lav, C., Haghiri, A., and Sandberg, R., "RANS predictions of trailing-edge slot flows using heat-flux closures developed with CFD-driven machine learning," *Journal of the Global Power and Propulsion Society*, Vol. 2021, No. May, 2021, pp. 1–13. https://doi.org/10.33737/jgpps/133114.

[60] Weatheritt, J., and Sandberg, R. D., "The development of algebraic stress models using a novel evolutionary algorithm," *International Journal of Heat and Fluid Flow*, Vol. 68, 2017, pp. 298–318. https://doi.org/10.1016/j.ijheatfluidflow.2017.04.004.

[61] Chu, J., *Experimental surface pressure data obtained on 65° delta wing across Reynolds number and Mach number ranges*, Vol. 1 - Sharp Leading Edge, National Aeronautics and Space Administration, Langley Rearch Center, 1996.

[62] Probst, A., and Reuß, S., "Progress in scale-resolving simulations with the DLR-TAU code," Deutscher Luft- und Raumfahrtkongress, Braunschweig, Deutschland, 2016.

[63] Shur, M. L., and al., "Turbulence Modeling in Rotating and Curved Channels:Assessing the Spalart-Shur Correction," *AIAA Journal*, Vol. 38, No. 5, 2000. https://doi.org/10.2514/2.1058.

[64] Peng, S.-H., "Verification of RANS and hybrid RANS-LES modelling in computations of a delta-wing flow," *46th AIAA Fluid Dynamics Conference*, 2016, p. 3480. https://doi.org/10.2514/6.2016-3480.